scientific reports

OPEN

Investigation of Bi$_2$MoO$_6$/MXene nanostructured composites for photodegradation and advanced energy storage applications

Sagarika Panda[1], Savita Mehlawat[1], Neeraj Dhariwal[1], Preety Yadav[1], Vinod Kumar[1], O. P. Thakur[1], Neha V. Brahmankar[2], Santosh J. Uke[2], Ashwani Kumar[3] & Amit Sanger[1]✉

This study presents nanostructured composite Bi$_2$MoO$_6$/MXene heterostructure by using hydrothermal method for photodegradation of the congo-red dye and also for energy storage devices. X-ray diffractometer (XRD), High Resolution Transmission Electron Microscopy (HRTEM), Field emission scanning electron microscope (FESEM) and X-ray photoelectron spectroscopy (XPS), Brunauer-Emmett-Teller (BET) were performed to examine the structural properties along with surface area and porosity of the material. Due to addition of MXene the larger surface area and improved pore size help to quickly break down additional organic pollutants by adsorbing them. The band gap of Bi$_2$MoO$_6$/MXene nanostructured composite reduced to 2.4 eV suggesting transfer of electrons from VB to CB. Bi$_2$MoO$_6$/MXene exhibits a high (92.3%) photocatalytic degradation rate for a duration of 16 min which was verified using UV-visible spectroscopy, also scavenger test was conducted to ascertain the reactive agent along with the degradation pathway was confirmed by LCMS. Elemental content was also established by using inductively coupled plasma mass spectrometry (ICP-MS). For estimating energy storage capacity cyclic voltammetry (CV) was performed. It was observed Bi$_2$MoO$_6$/MXene nanostructured composite electrodes had specific capacitance of 642.91Fg^{-1}, power density of 1.24 kWkg^{-1}, and energy density of 22.32 Whkg^{-1} at a current density of 5Ag^{-1} also it exhibited 64.42% capacity retention having current density 20 Ag^{-1} throughout 10,000 Galvanostatic charge discharge (GCD) cycles. High electrical conductivity of Bi$_2$MoO$_6$/MXene electrode was again examined by Electrochemical impedance spectroscopy (EIS). These findings demonstrate the potential of Bi$_2$MoO$_6$/MXene nanostructured composites in both photodegradation and energy storage applications.

Keywords Photodegradation, Congo-red, Energy storage, Solar irradiation, Electrodes

The existence of micropollutants in the aquatic habitat has developed into an enormous global environmental concern over a few decades. Known by another name, emerging contaminants, or micropollutants, are a wide range of both natural and man-made chemicals. Pharmaceuticals, cosmetics, steroid hormones, industrial chemicals, insecticides, and numerous other newly discovered substances are among them[1,2]. Before being released into the environment, antibiotic residues in water and wastewater can be treated using a variety of techniques. These techniques are again divided into 3 categories according to their principles of operations; physical removal, chemical degradation, and biological treatment[3,4]. Photodegradation is when a semiconductor's electrons are stimulated and travel from the valence band (VB) to the conduction band (CB) in response to light that exceeds its optical band gap, which results same amount of positively charged holes in the VB. When photogenerated electrons (e$^-$) and holes (h$^+$) on a semiconductor surface react with adsorption species (O$_2$, OH$^-$ etc.) on the catalyst surface, free radicals (.O$_2^-$, .OH etc.) are produced. These free radicals can operate as reactive species and break down the organic pollutants that have been adsorbed[5,6]. Here we used Congo red dye for the degradation process. Congo-red [sodium 3,3'-(1E, 1E')-biphenyl-4,4'-diylbis(diazene-2,1-diyl) bis(4-aminonapthalene-1-sulfonate)] is widely used diazo dye. High dissolved solids are present in Congo-red effluents, which are also brightly pigmented, have high chemical oxygen demand and low biological oxygen demand[7]. Benzidine is a toxic metabolite of the Congo-red that leads to carcinogenic, mutagenic, and allergic in

[1]Department of Physics, Netaji Subhas University of Technology, Dwarka, New Delhi 110078, India. [2]Department of Physics, JDPS College, SGB Amravati University, Amravati 444803, Maharashtra, India. [3]Department of Physics, Regional Institute of Education (NCERT), Bhubaneswar 751022, Odisha, India. ✉email: amit.sanger@nsut.ac.in

humans and animals, increases COD in water bodies and phototoxicity in plants[8]. Congo-red dye is incredibly resistant to deterioration because of its delicate structure and longevity. Therefore, several methods, including photochemical oxidation, adsorption, catalysis, coagulation, filtration, ozonation, electrochemical degradation, and photocatalytic degradation, are used to remove hazardous coloured dye from wastewater[9,10]. Because of photocatalysis's clean, affordable, sustainable, and ecologically friendly qualities, it has captivated heaps of research interest in recent decades as a solution to the growing problems with environmental pollution[11–13].

Finding clean, effective sources of energy and feasible energy storage facilities is necessary to meet the world's energy needs, which are also being exacerbated by the world's expanding population, changing lifestyles, and industrial advancements. The depletion of non-renewable sources of energy also has an irreversible detrimental influence on the environment. When compared to batteries and traditional capacitors, electrochemical supercapacitors have garnered a lot of attention because of their high-power density, quick charge and discharge cycles, long-term cyclic reliability, inexpensive cost, and simple maintenance[14,15]. Recently, materials such as BiOCl[16], Bi_2WO_6[17], activated carbon/BiOI, NiCuCoO[18], $WO_3/Bi_2MoO_6/rGO$[19], tungsten oxide/carbon nanocomposite[20], Carbon Dots/Bi_2MoO_6[15], CuO mixed with activated biochar[21], SnO_2-Bi_2WO_6[22] materials used for supercapacitors due to their high specific capacitance, energy density, and improved cycling stability. However, they have encountered certain challenges like low surface area, poor electrical conductivity, low rate in transfer of electrons etc. which has led researchers to seek out new composite materials that will overcome these challenges.

The past few years have noted a significant increase in research on two-dimensional (2D) MXenes, due to high metallic conductivity, outstanding structural stability, and mechanical flexibility[23–25]. MXenes has contributed to the research on biosensors, supercapacitors and rechargeable batteries[26–28]. Moreover, Ti_3C_2 MXenes' unique characteristics make it a potentially useful cocatalyst in the realm of photocatalysis: Ti_3C_2 MXenes have a lot of hydrophilic functionalities (O, F, OH) on their surface, which allows them to make good contact with a variety of semiconductors[29–31]. Ti_3C_2 MXenes' enhanced electroconductivity makes it an excellent electron sink that can readily trap photogenerated electrons, speeding up the segregation and transport of photoexcited charge carriers[24]. MXene has also been researched for the advancement of batteries, supercapacitors, and electronic shielding due to their properties like high electronic conductivity, high volumetric capacitance, and high mechanical strength[32,33]. In comparison to graphite anode, $Ti_3C_2T_X$ MXenes has less lithium diffusion barrier suggesting improved rate of Li^+ transport and large rate of lithiation/delithiation[34].

The Aurivillius family of Bi_2XO_6 (X-W or Mo), which is made up of alternating $(Bi_2O_2)^{2+}$ and $(XO_4)^{2-}$ perovskite layers, that has drawn a lot of interest among various photocatalysts due to the layered structures and exceptional physicochemical properties also this perovskite layers can be employed as an anode material for the lithium-ion batteries considering its theoretically high capacity along with low desertion potential[35,36]. Specifically, CB, VB, and suitable energy band gap of Bi_2MoO_6 make it a potential photocatalyst (CB)[37,38].

In this study, we used Bi_2MoO_6/MXene (Ti_3C_2) composite prepared by hydrothermal method which shows improvements in its properties and enhanced behaviour in dye degradation and supercapacitor applications. The combination of monolayer Bi_2MoO_6 and 2D stacked MXenes will result in a new 2D/2D Schottky heterojunction, which typically forms in between the metal and semiconductor interface. Furthermore, Schottky heterojunction has also been confirmed as a highly effective strategy and to accelerate photogenerated charge carrier transfer because of the inherent electric field that forms at the contact interface between monolayer Bi_2MoO_6 and MXenes which shows excellent reduction in photodegradation time in presence of sunlight. Additionally, this research on Bi_2MoO_6/MXene heterostructures highlights novel findings for the field of energy storage, excellent electrode material for supercapacitors and having enhanced excellent capacity retention. To the best of our knowledge this is the first report on super capacitive behaviour of Bi_2MoO_6/MXene material.

Experimental
Preparation of MXene (Ti3C2)
MXene was prepared from Ti_3AlC_2 MAX phase by etching the Al layer. 0.50 mg of Ti_3AlC_2 material was cautiously and gently added in 10 ml 40% HF solution by putting the mixture in a Teflon container and stirred vigorously at room temperature for 24 h (at room temperature 28 °C). After that it is centrifuged and then washed multiple times with deionized water (DI) and ethanol till pH reached approximately 6. At last, the MXene was dried in vacuum oven at 80 °C for about 24 h.

Preparation of Bi2MoO6
Bi_2MoO_6 was produced via hydrothermal technique. initially 2.43 g of Bismuth nitrate ($Bi(NO_3)_3.5H_2O$) mixed with 7.3 mL of ethanediol and 1.214 g of Sodium molybdate ($Na_2MoO_4.2H_2O$) mixed with 3.64 mL of DI and stirred independently for 30 min at a temperature of 55 °C. Hereafter both of them were mixed and stirred for 1 h at 55 °C. Then the solution was placed in the autoclave for 15 h at 150 °C. The product was then centrifuged, washed with the help of DI and then dried in vacuum oven for about 48 h to obtain Bi_2MoO_6.

Preparation of Bi2MoO6/MXene
Bi_2MoO_6/MXene (1:0.3 ratio of Bi_2MoO_6 and MXene) was developed via hydrothermal method without any other precipitating agent. 2.43 g of $Bi(NO_3)_3.5H_2O$ mixed with 7.3mL of ethanediol and 1.214 g of $Na_2MoO_4.2H_2O$ mixed with 3.64 mL of DI and stirred separately for 30 min at 55 °C. After that both of them were mixed and again stirred for 30 min at 55 °C, simultaneously 2 mg of MXene was sonicated with DI for 30 min. Then both the mixture was mixed and stirred vigorously again for another 30 min. The solution was then put in the autoclave for 15 h at 150 °C. The final outcome was then centrifuged and washed using DI and dried in the vacuum oven for about 48 h to obtain Bi_2MoO_6/MXene.

Fabrication of electrode

The substrates used to prepare the Bi_2MoO_6, MXene, and Bi_2MoO_6/MXene electrodes were grade 304 stainless steels (SS). SS was first washed with detergent and immersed in the 4 N HNO_3 and then cleaned with acetone and DI. Subsequently, the substrate was oven-dried. By applying a homogeneous layer to a SS substrate, a doctor blade was used to combine a mixture of the carbon black (acetylene black) and active material (prepared electrode material), poly (vinylidene fluoride) (PVDF) in weight percentages of 10%, 85% and 5% accordingly within dimethyl formamide (DMF). Thereafter electrodes were dried at 60 °C for overnight. Following heating, an electrode with a 1×1 cm^2 area weighed approximately of 2 mg.

Sample characterization

The crystallographic structure composition of Bi_2MoO_6/MXene was explored by using an X-ray diffractometer (XRD) (Bruker D2-Phaser). High Resolution transmission electron microscopes (HRTEM) (TALOS F200X G2), Field emission scanning electron microscope (FESEM) (Zeiss Ultra Plus) and Energy Dispersive X-ray spectroscopy (EDX) was used for investigating the cross-sectional view and surface morphology of the composition. Brunauer-Emmett-Teller (BET) (BELSORP-maxII) was performed to examine the surface area and porosity of the material. X-ray photoelectron spectroscopy (XPS) (PHI 5000 VersaProbe III) was utilized to study electrical and chemical states. Photocatalytic performance of sample was analysed by degradation of Congo-red dye and optical band gap values was evaluated with the help of UV-visible spectroscopy (Cary 60 UV-Vis). Further, inductively coupled plasma mass spectrometry (ICP-MS) (G3665A) was done to have a grasp of the elemental content in the degraded product along with liquid chromatography-mass spectroscopy (LCMS) (Agilent G6530AA (LC-HRMS-Q-TOF)) was performed to explore the degradation pathway. Cyclic voltammetry (CV) (EmStat4S.LR) was conducted to examined the electrochemical properties of the samples.

Photocatalytic degradation

The photocatalytic activities of sample are calculated through degradation of Congo-red of 5 mg/L under sunlight (The experiment was conducted during 11 a.m to 2 p.m. (mid of June, 2024) and the irradiation was about 340 WH/m^{2} [39]). 10 mg of photocatalysis was added to 50 mL of dye solution. At first, it was checked in dark environment, showed no degradation then placed under sunlight. The data was taken in every 4 min intervals. Thereafter, the deteriorated solution was utilized to analyse absorbance associated with the maximal absorption of Congo-red dye of wavelength 490 nm with the help of UV–visible spectroscopy. The degradation percentage of catalysts due to Congo red dye was calibrated by using Eq. (1).

$$\text{Percentage of degradation } (\%) = \frac{C_o - C}{C_o} \times 100 \tag{1}$$

where C_o and C stand for the solution's absorbance before and afterward exposition to sunlight respectively[40].

Electrochemical analysis

An electrochemical workstation (EmStat4S.LR) was used for electrochemical analysis. Using the manufactured electrode for the working electrode, an Ag/AgCl electrode for reference electrode and, a platinum electrode for counter electrode, an electrochemical cell was created for electrochemical characterization. For electrolyte, 1 molL^{-1} Na_2SO_4 aqueous solution was employed. The as-prepared electrodes were examined electrochemically using CV, GCD, and EIS electrochemical techniques. By combining the GCD and CV approaches, specific capacitance (Cs) (Fg^{-1}) was computed using Eqs. (2) and (3), respectively. Additionally, Eqs. (4), (5), and (6) were used to compute Power density (P_d) (Wkg^{-1}), Energy density (E_d) (Whkg^{-1}), and Coulombic efficiency.

$$Cs = \frac{1}{mv \left(V_{max} - V_{min}\right)} \int_{V_a}^{V_c} I\left(v\right) dv \tag{2}$$

$$c_s = \frac{I_d \times t_d}{\Delta V m} \tag{3}$$

$$E_d = \frac{0.5 \times c_s \left(V_{max}^2 - V_{min}^2\right)}{3.6} \tag{4}$$

$$P_d = \frac{E_d \times 3600}{t_d} \tag{5}$$

$$\eta = \frac{t_d}{t_c} \times 100 \tag{6}$$

where scan rate and the potential window (volts) are symbolized by 'V', '$(V_{max} - V_{min})$'. 'V_{max}' and 'V_{min}' refers cathodic and anodic current. 'm' denotes deposited mass (grams), and '$I(v)$' stands for current (milliamperes). t_d and I_d represent discharge current (s) and current density respectively. t_c and t_d indicates the electrode's charge and discharge time in GCD curve correspondingly.

Results and discussion

Structural exploration

XRD analysis was regulated to discern the composition of bare Bi_2MoO_6, MXene, and Bi_2MoO_6/MXene using an X-ray diffractometer as shown in Fig. 1 in order to understand more about the crystallographic and phase formation of the synthesized materials. The diffraction peaks of MXene were observed corresponding to (002), (004), (110) crystallite planes[41]. The XRD pattern of Bi_2MoO_6 nanoplates comprises sharp peaks corresponding to the (140), (131), (002), (220), (222), (113). The position of all peaks matched with the orthorhombic crystal system of Bi_2MoO_6 (JCPDS reference code 21-0102). Characteristic peaks of Bi_2MoO_6 and MXene are observed in Bi_2MoO_6/MXene nanostructured-composite suggesting the fact that MXene were decorated on the surface of Bi_2MoO_6.

Morphological investigation

Figure 2a of the TEM picture of MXene revealed that the material had a transparent, flat monolayer surface with a lattice spacing of 1.02 nm, which corresponds to the (002) plane[42,43]. Also, Fig. 2b presented the TEM picture of Bi_2MoO_6 with a lattice spacing of 0.26, that corresponded to the (002) plane. Multiple Bi_2MoO_6 particles were embedded or coated on the MXene nanosheet, as seen in the Bi_2MoO_6/MXene also heterojunctions are formed by layered MXene and Bi_2MoO_6 components, as confirmed by the TEM images shown in Fig. 2c. The close interactions among Bi_2MoO_6 and MXene was further demonstrated by the lattice arrangement of the HRTEM picture of the binary heterojunction. Figure 2(c_1) illustrated the MXene sheet of plane (200) matched the lattice spacing of d = 1.02 nm. Again, the lattice spacing of d = 0.268 nm and d = 0.322 nm corresponded to plane (002) and (131) respectively of Bi_2MoO_6 (Fig. 2(c_2))[44,45].

FESEM was carried out to verify surface morphology of bare Bi_2MoO_6, MXene and Bi_2MoO_6/MXene as represented in Fig. 2. The FESEM image of MXene (Fig. 3a) indicates that it has a typical accordion-like structure[46,47].Prepared bare Bi_2MoO_6 shows an irregular nanoplate-like morphology as seen in Fig. 3b corresponding to the Orthorhombic Crystal system. Figure 3c shows that Bi_2MoO_6 nanoplates possessing their uneven structure have been settled on the MXene nanosheets. Due to the addition of MXene, which may result
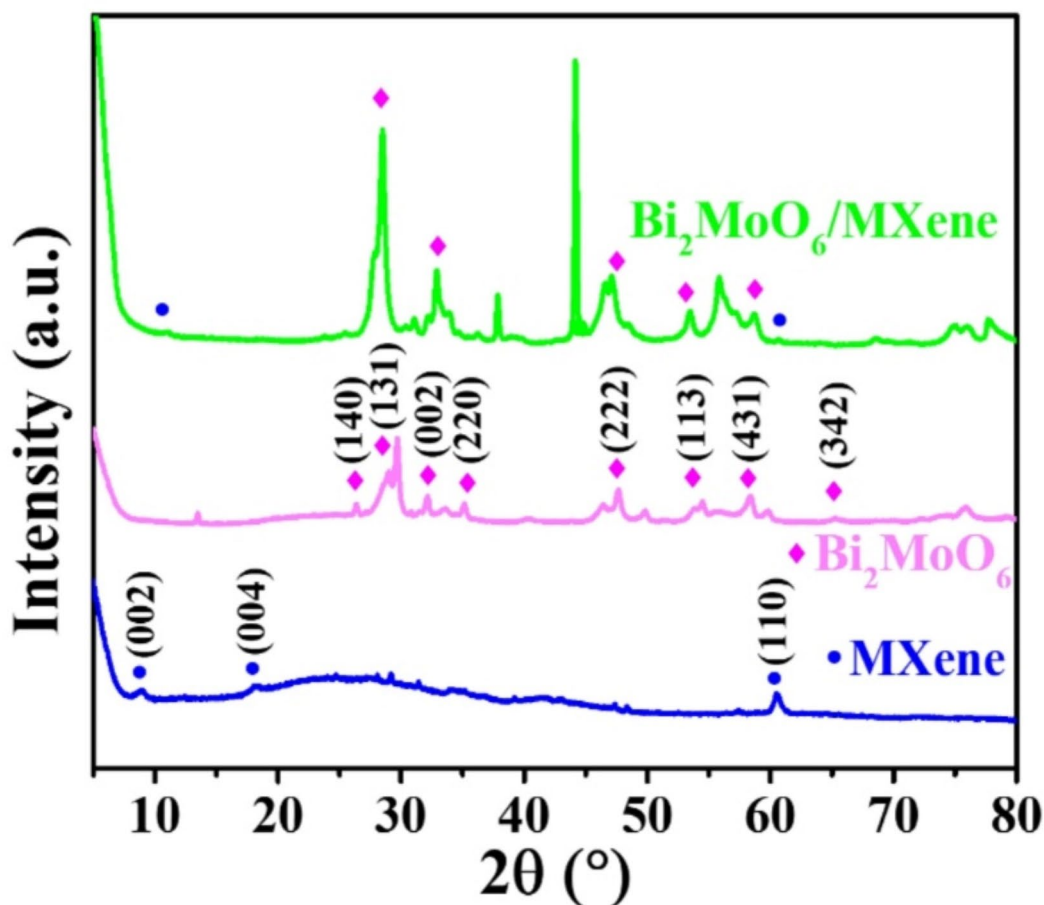

Fig. 1. XRD patterns for MXene nanosheet, bare Bi_2MoO_6 nanoplates and Bi_2MoO_6/MXene.

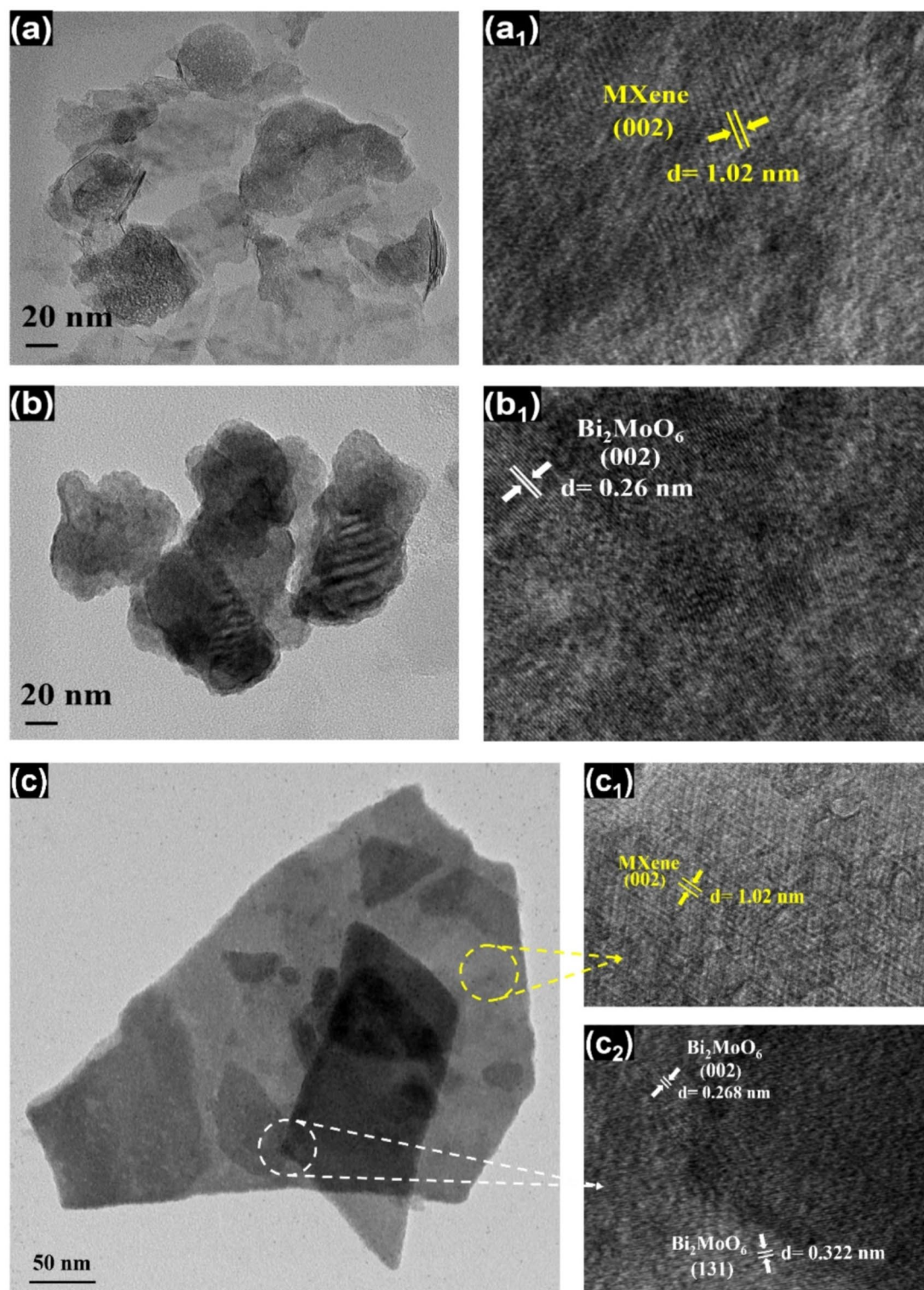**Fig. 2**. HRTEM image of (**a**), (**a₁**) MXene nanosheet with d spacing (**b**), (**b₁**) bare Bi_2MoO_6 nanoplates and the d spacing (**c**),(**c₁**), (**c₂**) Bi_2MoO_6/MXene with respective d spacing of individual.

in the creation of nucleation sites for Bi_2MoO_6 and thereby stop additional crystal growth, that attributed to the enhancement of pore size distribution of the Bi_2MoO_6/MXene nanostructured composite than that of Bi_2MoO_6 and MXene (as from BET analysis).

In addition, EDX spectra are also characterized which shows the elemental mapping over a scanned area. Figure 4a shows the EDX spectra with elemental concentration of MXene which composes 13.99 at% of C, 43.70 at% of F and 42.31% of Ti. Figure 4b shows the EDX spectra with elemental concentration of bare Bi_2MoO_6
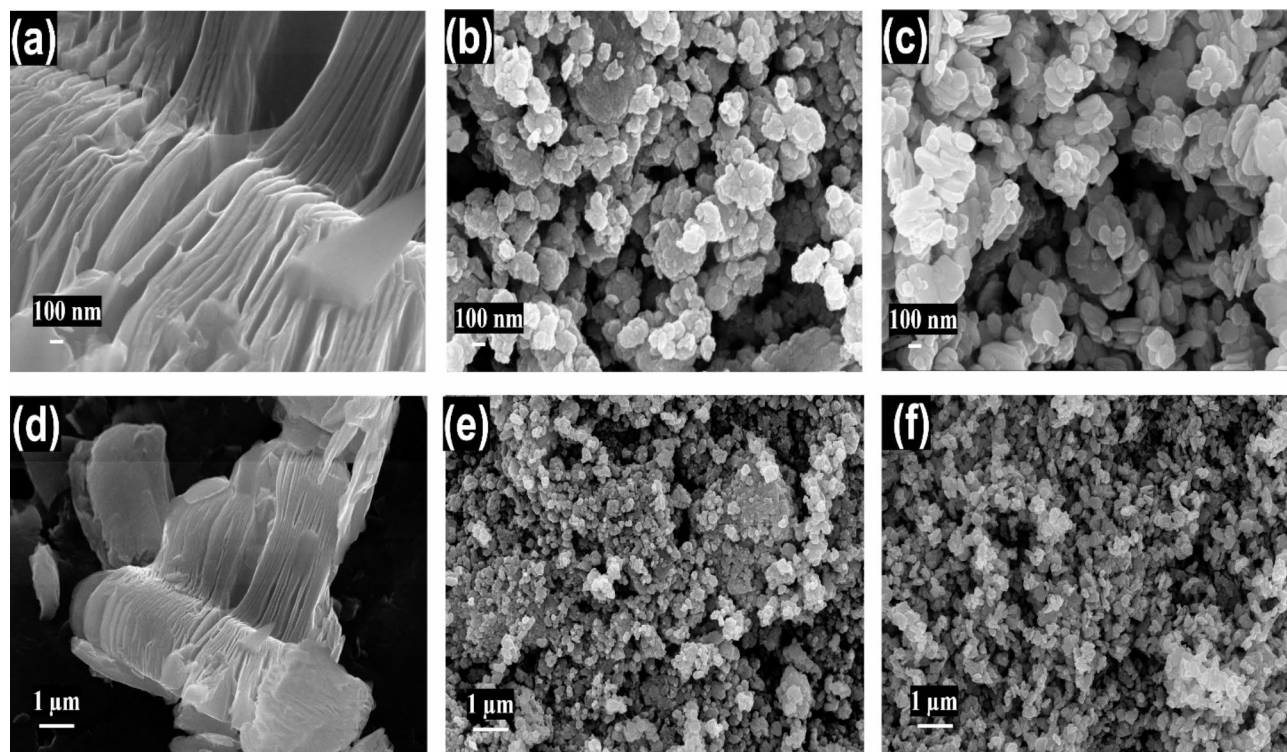
Fig. 3. FESEM scans for (**a**) MXene nanosheet (**b**) Bare Bi_2MoO_6 nanoplates (**c**) Bi_2MoO_6/MXene respectively.
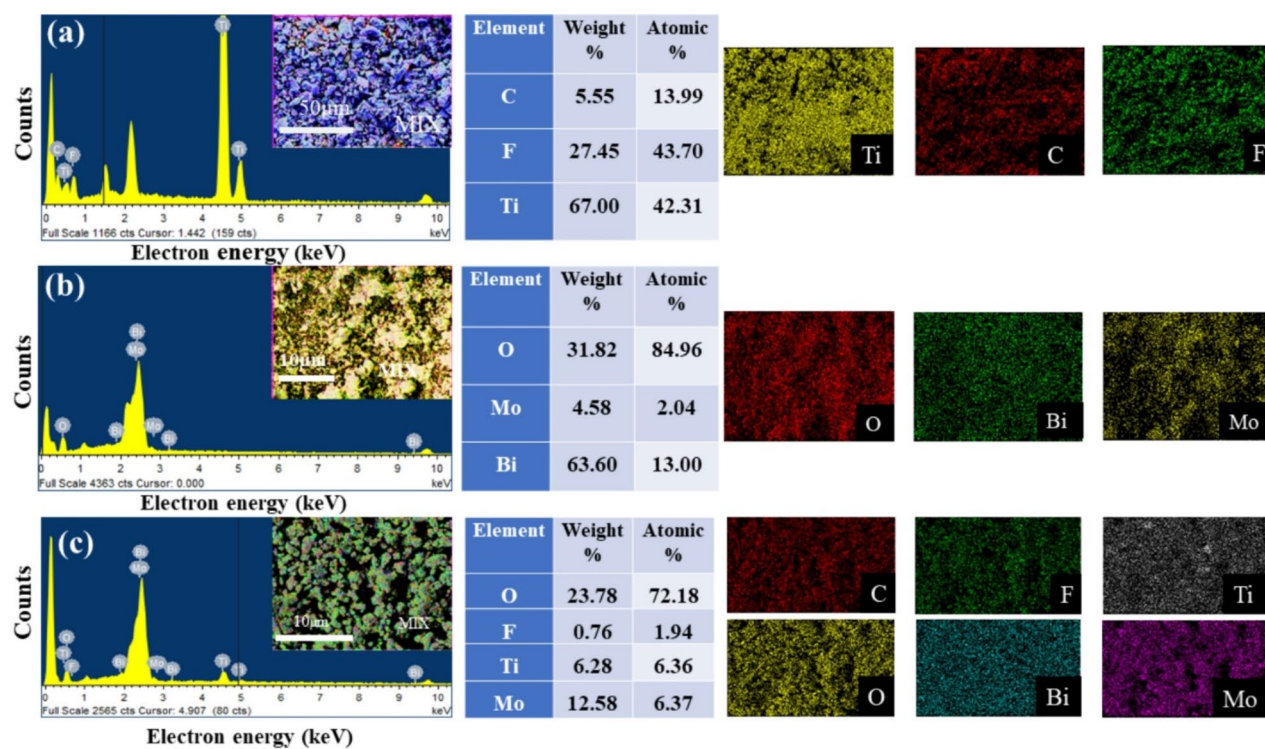

Fig. 4. EDX spectra of (**a**) MXene, (**b**) Bi_2MoO_6, and (**c**) Bi_2MoO_6/MXene alongside elemental mapping.

which exhibits 84.96 at% of O, 2.04 at% of Mo, and 13% Bi. Figure 4c shows the EDX spectra with elemental concentration of Bi_2MoO_6/MXene which exhibits 72.18 at% of O, 1.94 at% of F, 6.36% of Ti, and 6.37 at% of Mo. Also, Fig. 4 illustrates the mixed electron image of all presented, the colour map of all individual composites that are present in the elements of MXene, bare Bi_2MoO_6, and Bi_2MoO_6/MXene.

BET analysis

From BET analysis, the detailed surface characteristics and pore volume of the obtained nanomaterials were ascertained using the nitrogen-sorption isotherm; the outcomes are displayed in Fig. 5(a-c). The isotherm is categorized as a type II isotherm with a broad range of pore sizes by the IUPAC. The surface area of MXene, Bi_2MoO_6 and Bi_2MoO_6/MXene was found to be 6.053, 24.821, 67.3 m^2g^{-1} and pore size was 4.9, 13.5, 16.2 nm respectively. Along with pore volume was calculated to be 0.084, 0.117 and 0.281 $cm^3 g^{-1}$ for MXene, Bi_2MoO_6 and Bi_2MoO_6/MXene. BET results reveal that Bi_2MoO_6/MXene is more porous than Bi_2MoO_6, MXene due to its larger surface area and improved pore size. Because of this tendency, it can quickly break down additional organic pollutants by adsorbing them. Consequently, the porous nature of the material led to a rapid dispersion of reactants and products, increasing the rate of the photocatalytic process.

XPS studies

Figures 6a and 7a, and 8a indicate the XPS spectra of, MXene, Bi_2MoO_6 and Bi_2MoO_6/MXene which accords with the outcome of EDX. After the amalgamation of Bi_2MoO_6, C–Ti bond evanesces, intimating that C–Ti bond was demolished during process of synthesis and other peaks presented at 284.5, 286.1 eV accredit to C-C and C-O bond. XPS of Ti 2P of MXene (Fig. 6b); can be ascribed to Ti-C $2p_{3/2}$, Ti(II) $2p_{3/2}$, Ti(III) $2p_{3/2}$, Ti(IV) $2p_{3/2}$ having seven peaks positioned at 454.6 (460.8), 455.1 (462), 456.2 (464.1) and 459.2 eV, where the intensity of Ti (IV) is weakest[48]. Four peaks manifest in C 1s spectrum of MXene (Fig. 6c) at 281.7, 284.7, 285.5, and 288.9 eV, that attributes to the C–Ti, C–C, C–O, and C–F bonds respectively[49]. The Bi 4f spectra of pure Bi_2MoO_6 illustrated in Fig. 7b, are an adherent of binding energies of Bi $4f_{7/2}$ and Bi $4f_{5/2}$ of Bi^{3+}[50], also additional 5 peaks shoot up at 156.96 eV, 157.96, 159.92, 163.11, and 164.95 eV while in the case of Bi_2MoO_6/MXene the Bi 4f spectra (Fig. 8b) positioned at157.25, 158.46, 158.97, 163.97 and 165.56 eV. A glimpse 2 peaks of Bi_2MoO_6 (Fig. 7c) at 231.01 and 234.33 eV are allotted to binding energies of Mo $3d_{3/2}$ and Mo $3d_{5/2}$ of Mo^{6+}[51], but Mo 3d peaks of Bi_2MoO_6/MXene (Fig. 8c) appear at 230.2, 231.5, 234.6, and 235.01 eV, respectively. Figure 7d manifests the O 1s spectrum of pure Bi_2MoO_6 having peaks at position 529 and 530.9 eV ascribed to Bi-O and Mo–O[51] but in Bi_2MoO_6/MXene (Fig. 8d) the three peaks designated to Bi–O, Mo–O, and C–O are stationed at 529.8, 530.6, and 531.5 eV respectively. From Figs. 2 and 8e peaks of Ti 2p were observed for Bi_2MoO_6/MXene at 457.8 and 465.1 eV as well as 2 peaks of C 1s at 284.5, 286.12 eV (Fig. 8f) attributed to C-C and C-O bond respectively. Figure 8a illustrates the full XPS spectra of Bi_2MoO_6/MXene composite. Modifications in the locations of the VB and CB edges may be connected to this rise in binding energy in the Bi_2MoO_6/MXene composite that causes transfer of electrons from Bi_2MoO_6 to MXene by increasing electron density ultimately help in degradation process.

Optical properties

To scrutinize the optical phenomenon of Bi_2MoO_6 and Bi_2MoO_6/MXene, UV–visible spectroscopy was employed. The absorbance of sample was explored in the range 190 to 800 nm. Bi_2MoO_6/MXene evidenced a stronger light absorption than pure Bi_2MoO_6. The band gap of MXene was found to be 1.25 eV (Fig. 9a), furthermore, the band gap of Bi_2MoO_6 was calculated as 3.1 eV (Fig. 9b), which constricts to 2.4 eV after mixing with MXene as shown in Fig. 9c, calculated using Tauc's plot. In Tauc's plot photon energy (hν) is plotted against $(\alpha h\nu)^2$. The mechanism that is accountable for constricting the gap in bands associates the movement of electrons between top end of VB towards bottom end of CB. The composite material also exhibits increased absorbance across a wide wavelength range due to its reducing band gap.

Photocatalytic analysis

Figure 10a illustrates photodegradation of congo-red dye using MXene, which showed almost no degradation during the interval of 4 to 16 min. The photocatalytic abilities of synthesized Bi_2MoO_6/MXene (Fig. 10c) show

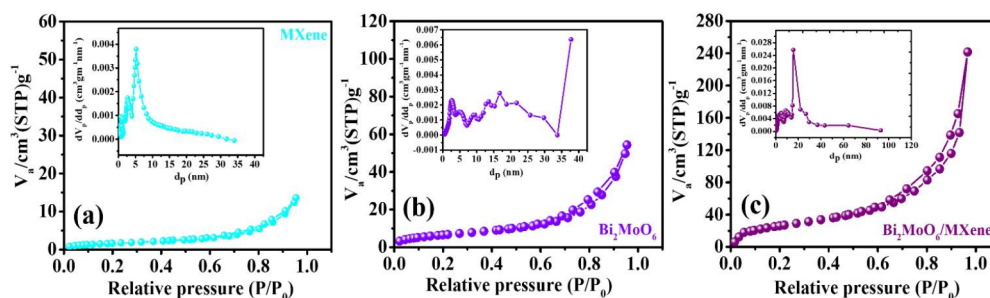**Fig. 5.** N_2-sorption isotherm of (**a**) MXene, (**b**) Bi_2MoO_6, (**c**) Bi_2MoO_6/MXene along with pore size distribution.
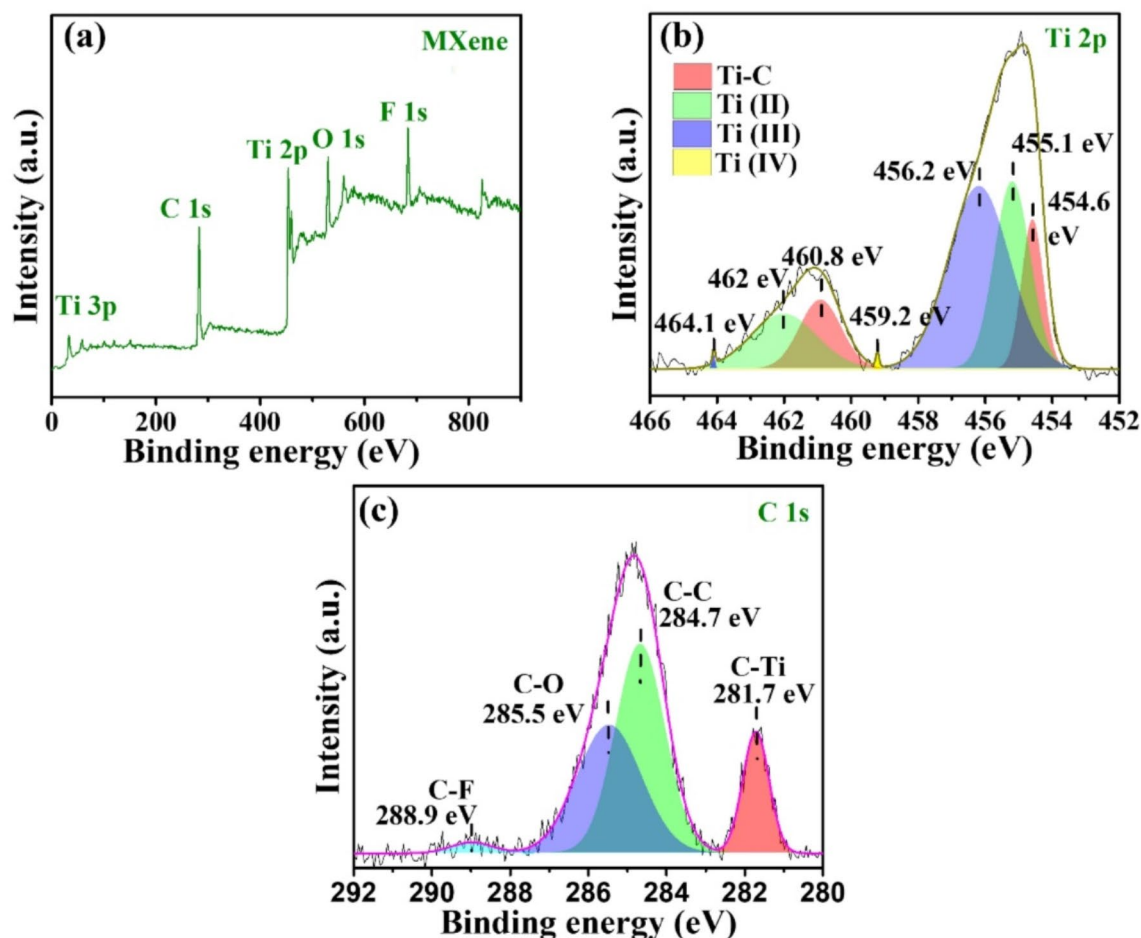
Fig. 6. (**a**) Full XPS of MXene and high-resolution spectrum of (**b**) Ti 2p, and (**c**) C 1 S.

degradation of 50 mg/L Congo-red dye under the daylight which shows a greater result when degraded with bare Bi_2MoO_6(Fig. 10b). When MXene was added with Bi_2MoO_6 it enhances the electron-hole separation in its band gap by forming energy states. Due to the existence of these impurity levels, additional energy levels are generated in the semiconductor's bandgap. Holes can remain at the valence band while electrons stimulated into the energy levels beyond the valence band. Then in order to hinder these excited electrons to recombining with holes that exist in valence band, they remain trapped within the impurity level. As in consequence, recombination speed of the electron-hole pair decreases with accelerating the rate of degradation. Photocatalytic degradation of MXene, bare Bi_2MoO_6 and Bi_2MoO_6/MXene is calculated using Eq. (1), which shows that only 8.3%, 60.5% of the dye degrades by MXene and pure Bi_2MoO_6 in 16 min under sunlight but using MXene 92.3% dye degrades in 16 min (Fig. 10d). Figure 10e illustrates that first the solution of pure Bi_2MoO_6 and Bi_2MoO_6/MXene were placed in dark room then transferred under sunlight. It was observed that in dark condition no degradation took place and proved to be a good catalyst under natural sun light irradiation. The mechanism behind photodegradation is, that when Bi_2MoO_6 is exposed to sunlight electrons will drift from its conduction band to MXene because of low fermi level in Bi_2MoO_6, establishing a Schottky junction at their interface. Such movement hinders the photo-induced e^-/h^+ pair from recombination[52].

Pseudo first order kinetic analysis of photodegradation of pure Bi_2MoO_6 and Bi_2MoO_6/MXene were analysed as shown in Fig. 10f. The kinetics data was calculated by using the Eqs. (7),

$$ln\frac{C}{C_0} = -Kt \qquad (7)$$

Here, C_0 and C denotes as concentration of targeted pollutants initial and after some time, k is pseudo first order kinetic rate constant in unit of min^{-1} and t is the processed time in $min^{53,54}$. From the Fig. 10f it is observed that the reaction rate of Bi_2MoO_6/MXene is 0.158 min^{-1} which is 2.6 times greater than bare Bi_2MoO_6 with regression coefficient 0.994. Further for MXene reaction rate is 0.013 min^{-1} having a regression coefficient of 0.945. This data again confirmed that the degradation rate is faster in addition of MXene. ICP-MS was performed to determine the content of bismuth (Bi), Molybdenum (Mo), Titanium (Ti), and fluorine (F) in the solution
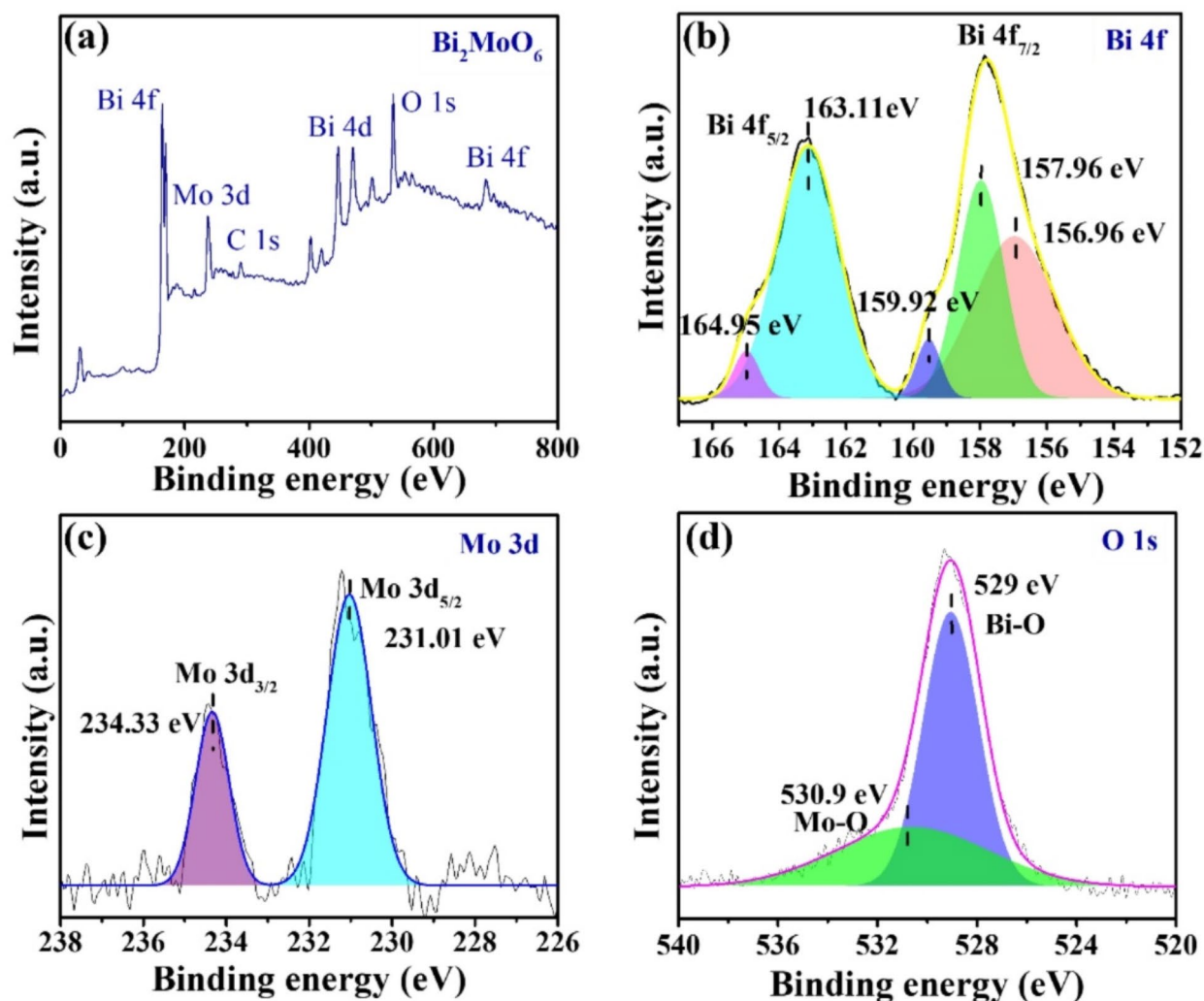
Fig. 7. (**a**) Full XPS spectra of Bi_2MoO_6, and high-resolution spectrum of (**b**) Bi 4f, (**c**) Mo 3d, and (**d**) O 1s.

both before and after degradation. From Fig. 10(g), it has been illustrated that even after degradation the metal content remains relatively unchanged.

Effect of degradation with variable concentration of dye

The degradation of varying dye concentrations from 2.5 mg/L to 30 mg /L was performed in the dark and then under sunlight as depicted in Fig. 11a. The outcomes indicated 91% degradation persisted up to addition of 10 mg congo-red dye but after that the degradation rate dropped. The rate of degradation is associated to the h^+ generation both in catalyst and in dye. Increased dye concentration results in larger average dye aggregate sizes, which reduces the amount of surface area exposed to environmental conditions that cause photodegradation. Thus, higher dye concentrations cause aggregation, which in turn causes slower photofading rates[55]. As in this situation, when the dye concentration increases (while maintaining the same amount of catalyst) the degradation rate decreases, at high concentrations.

Effect of degradation with variable catalyst dosage

Through altering the amount of photocatalyst dosage from 5 to 35 mg the degradation was accomplished in dark and then under sunlight. It has been observed from Fig. 11b that quicker degradation occurred with an increase in the dosage of the catalyst while maintaining the same concentration of dye. This is because of the active sites present in Bi_2MoO_6/MXene increases which are key to degradation. Higher catalyst dosage can absorb greater quantities of incident light which enhances the electron hole pair generation.

Effect of variable temperature on degradation process

Figure 11c shows the plot of percentage degradation of catalyst under variation of temperature from 0 to 70 °C. From the graph, it has been clarified that there is no such compelling variability in the degradation relating to
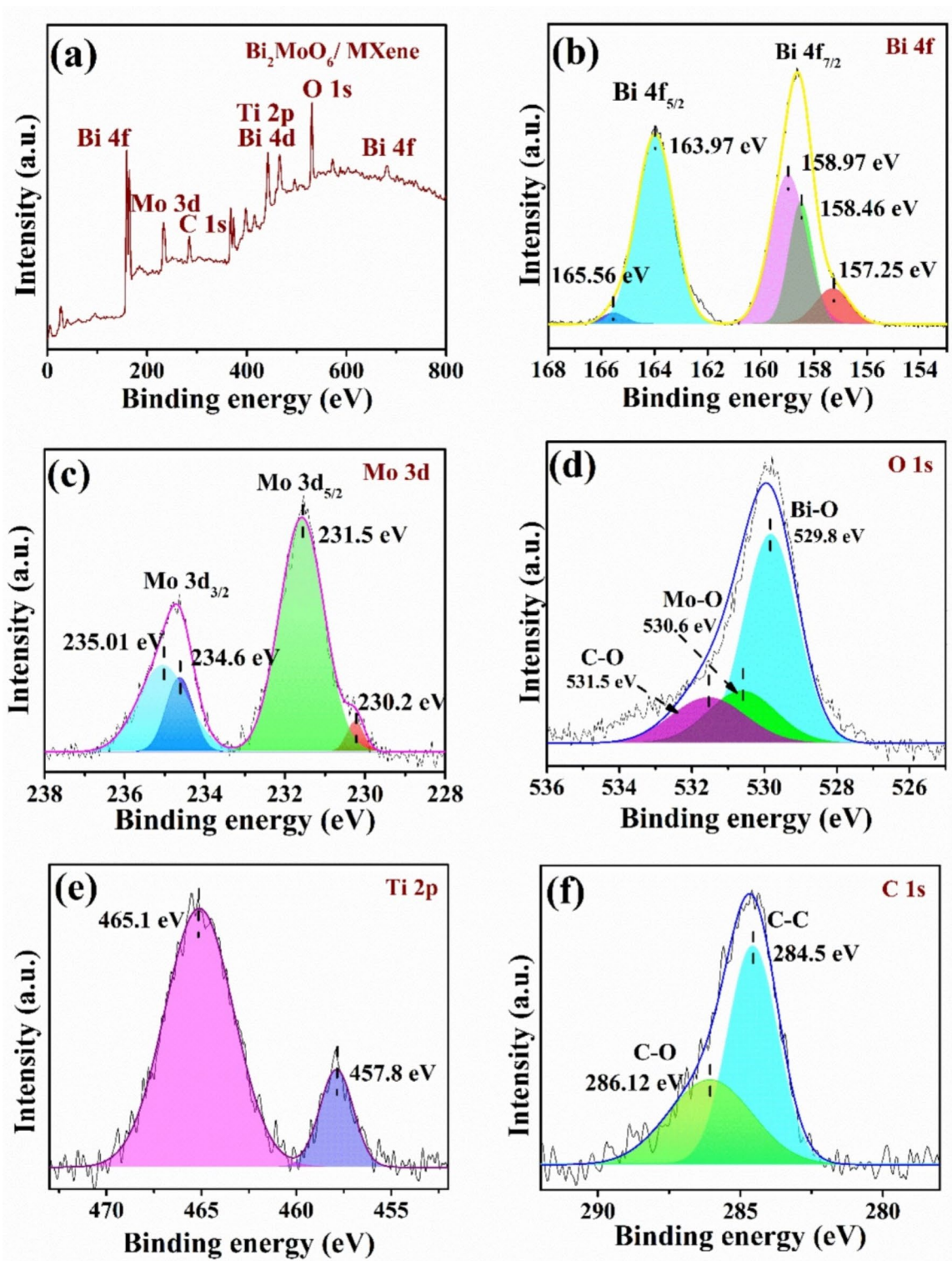
Fig. 8. (**a**) Full XPS spectra of Bi_2MoO_6/MXene, and high-resolution spectrum of (**b**) Bi 4f, (**c**) Mo 3d, (**d**) O 1s, (**e**) Ti 2p, and (**f**) C 1s.

differ in temperature, which comes up with fine confirmation that changes in temperature is ineffectual to the photocatalytic degradation.

Effect of various trapping agent

To diagnose the reactive element that helped in photodegradation of Congo-red scavenger test was performed. For photocatalytic degradation h^+, $.O_2^-$, $.OH$ plays a vital reactive agent[56,57]. In this paper isopropanol (IPA),

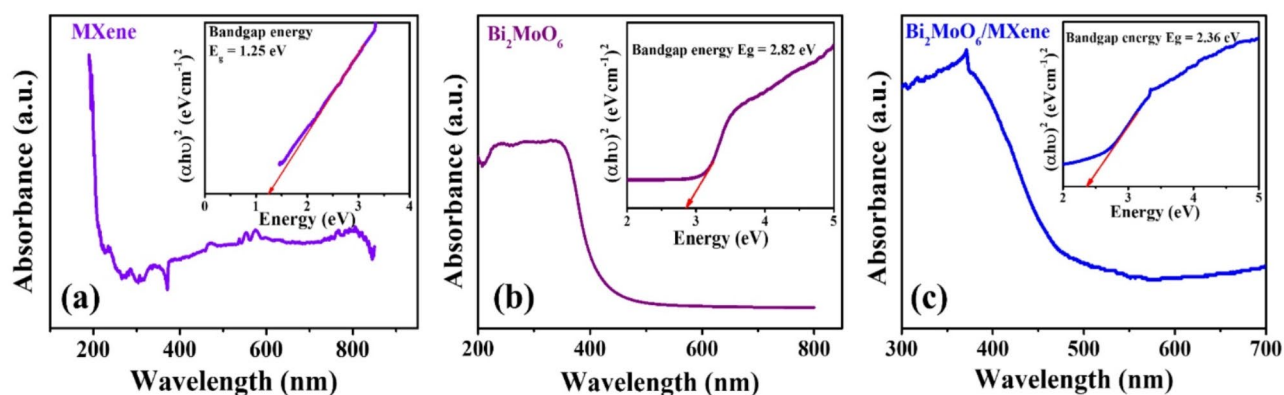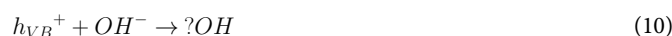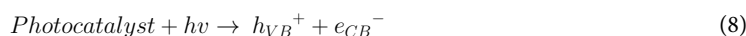**Fig. 9**. (**a–c**) UV- visible absorbance spectra and Tauc plot of MXene, Bi_2MoO_6 and Bi_2MoO_6/MXene respectively.

Formic acid (FA) and Benzoquinone (BQ) were used to eradicate .OH, h^+ and .O_2^- correspondingly. To perform the experiment same molarity of scavengers was taken (0.5 M). 50 ml of scavenger was added to 50 ml of Congo-red solution with 10 mg of catalyst and exposed to sunlight. It is observed from Fig. 11(d) that without scavenger the photocatalytic degradation is 92.3% while in adding up IPA, BQ, and FA the percentage of degradation fall off to 73%, 54% and 23%. This data shows that FA has relatively low ability in photodegradation in comparison with IPA and BQ.

Figure 12 demonstrates a probable photocatalytic mechanism of Bi_2MoO_6/MXene as determined from the above experimental results. Bi_2MoO_6 compound recognized for its photocatalytic activity in visible light. When exposed to light, it absorbs photons, promoting electrons from the VB to the CB, thereby generating electron-hole pairs. On the other hand, MXene, a family of two-dimensional transition metal carbides or nitrides, boasts high electrical conductivity and surface area. This unique structure plays a crucial role in enhancing charge separation and transport. MXene can prevent the electron-hole pair recombination as it comprises of electron traps. These photoinduced can convert O_2 to .O_2^-, a potent oxidant that degrades organic dyes. The pollutants can be directly oxidized to safe products via holes developing at VB of Bi_2MoO_6, that react with OH^- to generate .OH. Further, when .O_2^- and .OH reacted with Congo-red dye it breaks down to multiple molecules and finally degrades to CO_2 and H_2O with some nano particles. The following is the expression of every pertinent reaction:

$$Photocatalyst + hv \rightarrow h_{VB}^+ + e_{CB}^- \tag{8}$$

$$O_2 + e_{CB}^- \rightarrow ?O_2^- \tag{9}$$

$$h_{VB}^+ + OH^- \rightarrow ?OH \tag{10}$$

$$h^+/?O_2^-/?OH + Congo-red \rightarrow H_2O + CO_2 + nanoparticles \tag{11}$$

LC-MS was carried out to fully comprehend degradation procedure and to determine the decolorized final outcomes of congo-red dye during degradation when exposed to sunlight presented in Fig. 13c and the presumed degradation product during 4 min and 16 min are illustrated in Fig. 13a, b respectively. Congo-red firstly goes through asymmetric cleavage, that results in a couple of molecules (4-amino-3-diazenylnapthelene-1-sulphonate) with m/z value 273.1 along with one biphenyl diamine molecule having m/z 185.1. Subsequent dissociation of (4-amino-3-diazenylnapthelene-1-sulphonate) yields a couple of compounds at m/z 205.5 and m/z 157.08 which again dissociates to m/z of 143.07. Benzidine again dissociates and forms a compound having m/z 197.07, then again it dissociates having m/z of 211.09 after that to 183.06. Along with this, intermediates having m/z values 197, 232.07, 227, 210, 60.08, and 74.06 have been found. Consequently, it had been concluded from the outcomes that congo-red dye within an aqueous solution can be mineralized with the help of Bi_2MoO_6/MXene. A comparison on recent advancements of photocatalytic material for dye degradation along with Bi_2MoO_6/MXene nanostructured composite is shown in Table 1.

From this study it has been observed that addition of MXene has a greater impact on the composite. Numerous hydrophilic functionalities (O, F, and OH) on the surface of Ti_3C_2 MXenes enable them to form strong bonds with a range of semiconductors and also contribute to the composite's excellent dispersion in water. MXene's improved electroconductivity makes it a great electron sink that can easily capture photogenerated electrons, accelerating the separation and movement of charge carriers that have been photoexcited. According to BET studies, Bi_2MoO_6/MXene has a higher surface area and better pore size than Bi_2MoO_6, MXene, making it more porous. Its propensity to adsorb more organic contaminants allows it to degrade them more rapidly. These modified heterostructures should have a low rate of recombination, a suitable bandgap, improved charge carrier separation, and sufficient surface area to increase photocatalytic activity[58].
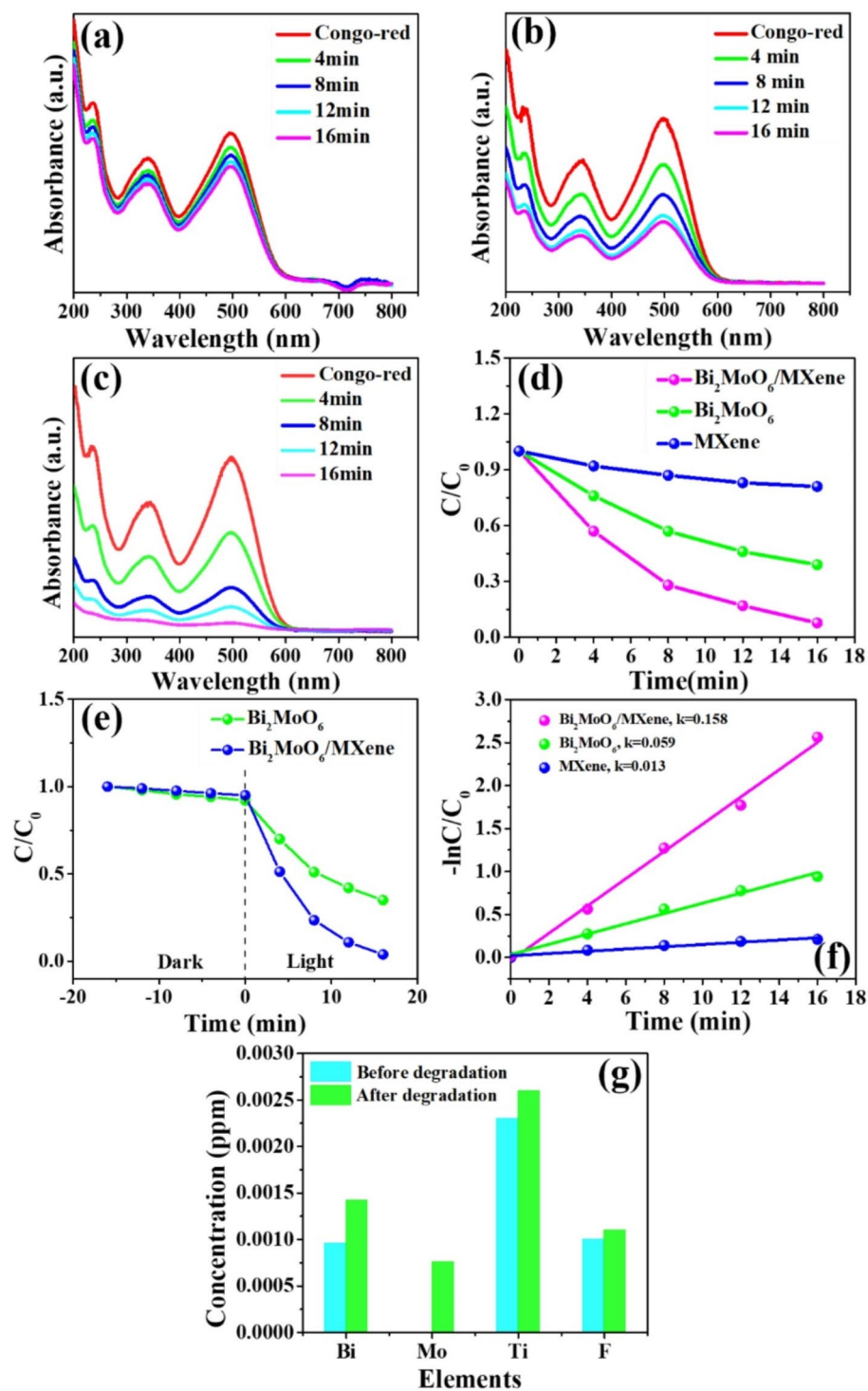
Fig. 10. (**a**–**c**) UV-visible spectra of degradation of Congo-red dye with MXene, Bi_2MoO_6, and Bi_2MoO_6/ MXene, (**d**) Photocatalytic degradation under sunlight, (**e**) Degradation absence and presence of light, (**f**) pseudo first order kinetics graph (**g**) Metal quantity in the solution both before and after degradation.

Electrochemical characteristics

The mechanism of a three-electrode supercapacitor involves the interaction between the working, counter, and reference electrodes, enabling precise measurement and optimization of electrochemical processes. Working Electrode is the main site for charge accumulation and electrochemical reactions, Counter Electrode Complements the working electrode by balancing the charge during the electrochemical processes and reference
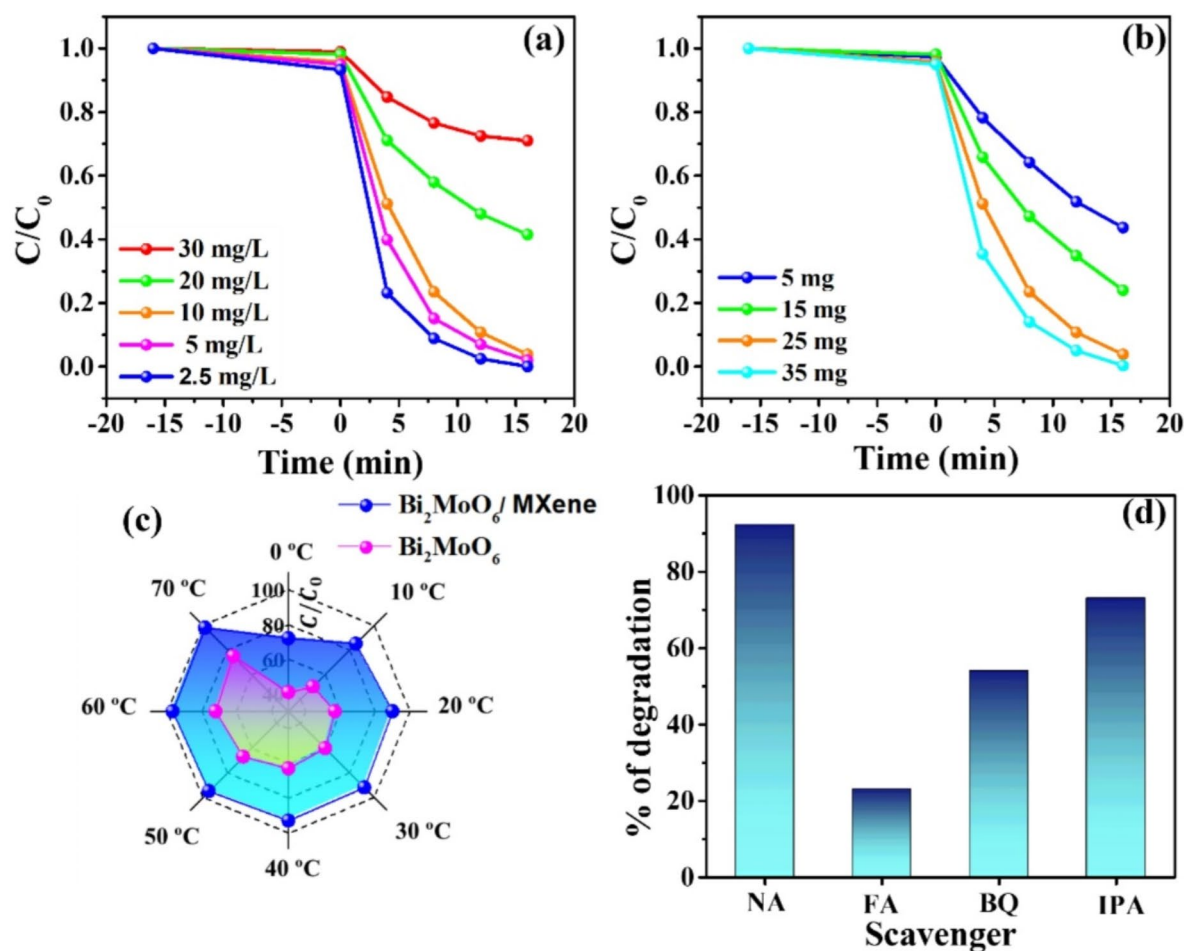
Fig. 11. (**a**) Degradation with variable concentration of Congo-red dye, (**b**) Degradation with variable photocatalyst dosage, (**c**) Degradation of Bi_2MoO_6, and Bi_2MoO_6/MXene with variation of temperature, (**d**) Radical trapping test using different scavengers for photo catalytic activity.

Electrode Provides a stable reference potential. Ions from the electrolyte migrate toward the electrodes in response to an applied voltage, creating an electric double layer across the interface. Electrochemical capacitors that store the charge electrostatically by using reversible adsorption of ions of electrolyte onto the active materials that have high accessible specific surface area and are electrochemically stable. At the working electrode, cations from the electrolyte are attracted to the negatively charged surface, while anions migrate to the counter electrode. Gouy and Chapman, and Stern and Geary, later improved the capacitance model by suggesting the presence of a diffuse layer in the electrolyte due to the accumulation of ions close to the electrode surface. Upon closing the circuit, ions return to the electrolyte, allowing electrons to flow through the external circuit, releasing stored energy[59,60].

Cyclic voltammetry (CV) analysis

CV was used to analyse electrochemical properties of the as-prepared MXene, Bi_2MoO_6, and Bi_2MoO_6/MXene electrodes. Figure 14a–c shows the relative CV curves for the fabricated MXene, Bi_2MoO_6, and Bi_2MoO_6/MXene electrodes. The CV investigation used 1 mol L^{-1} Na_2SO_4 liquid electrolyte having potential window of 0–0.5 V along with Ag/AgCl electrodes been scanned at 5-100 mVs^{-1}. The CV curves' distorted behaviour in Fig. 14a–c confirms the pseudocapacitive characteristic of energy storage appliance of the sample as they were processed. Furthermore, it is evident from Fig. 14a–c that an increase in the scan rate is accompanied by inflation in the current inside CV curves. Specific capacitance was calculated from the CV curves, using Eq. (2). The computed Cs values, E_d, and P_d at different scan rates for the MXene, Bi_2MoO_6 and Bi_2MoO_6/MXene electrodes are shown in Table 2. The electrode had high Cs (859.14 Fg^{-1}), E_d (29.83 Wh kg^{-1}) at 5 mVs^{-1} obtained for Bi_2MoO_6/MXene electrodes which is superior to the other MXene, Bi_2MoO_6 electrodes. Additionally, Fig. 15a provides a graphic representation of the variation in specific capacitance with scan rate. As the scan rate enhanced, specific capacitance decreased, as shown in Fig. 15a. The Bi_2MoO_6/MXene electrodes exhibited the highest specific capacitance value owing to its superior electrical conductivity, uniform porosity and enhanced surface area.
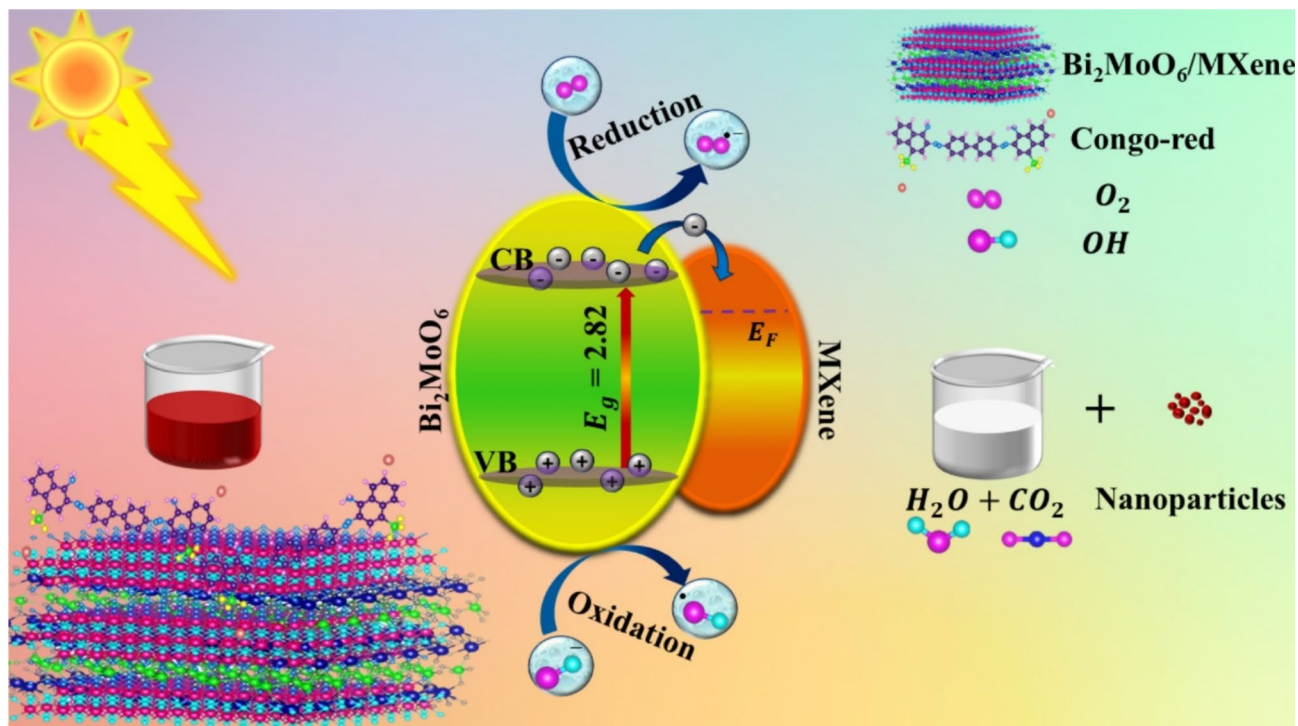
Fig. 12. Mechanism of photodegradation activity of Congo-red dye using Bi_2MoO_6/MXene under sunlight.

Galvanostatic charge discharge (GCD) analysis

To further study electrochemical behaviour and to evaluate the energy storage capacity of MXene, Bi_2MoO_6 and Bi_2MoO_6/MXene nanostructure composite electrodes, GCD analysis was performed. Ag/AgCl electrodes were used in this investigation, which covered a current density ranging from of 5–25 Ag^{-1}, using 1 mol L^{-1} Na_2SO_4 liquid electrolyte and a voltage range of 0–0.5 V Vs. Figure 14d–f shows the GCD curves of MXene, Bi_2MoO_6, and Bi_2MoO_6/MXene electrodes. The arbitrary behaviour of the GCD curves for the MXene, Bi_2MoO_6, and Bi_2MoO_6/MXene nanostructure composite electrodes is evident, suggesting that the energy storage is pseudocapacitive in nature. From GCD curves, the values of the specific capacitance obtained for MXene, Bi_2MoO_6, and Bi_2MoO_6/MXene nanostructure composite electrodes using Eq. (3) having current density density 5–25 Ag^{-1} are shown in Table 3. At current density 5Ag^{-1}, the Bi_2MoO_6/MXene electrode exhibited an impressive Cs of 642.91 Fg^{-1}, E_d of 22.32 Wh kg^{-1}, and P_d of 1.24 kW kg^{-1}. Figure 15b shows the graphical representation of the relationship in between specific capacitance and current density. As shown in Fig. 15b, the specific capacitance values dropped at higher current densities that is caused by the smaller availability of the electrolyte ions during fast-scanning settings. In addition, analysing the cycle stability is essential for determining the robustness and efficiency of electrodes ready for use in supercapacitors. Using the specific capacitance calculated from the GCD curve, the energy density and power density of the as prepared electrodes were calculated from the Eqs. (4) and (5). Furthermore, Fig. 15c shows the Ragone plot or the power density change P_d with respect to E_d for the MXene, Bi_2MoO_6 and Bi_2MoO_6/MXene electrodes Fig. 15d shows the percentage retention of capacitance with the cycle number for the Bi_2MoO_6/MXene electrode. Bi_2MoO_6/MXene electrode exhibited 64.47% capacity retention having 20Ag^{-1} density. A comparison on recent advancements on super capacitive material with Bi_2MoO_6/MXene nanostructured composite is shown in Table 4.

Electrochemical impedance spectroscopy (EIS)

The MXene, Bi_2MoO_6 and Bi_2MoO_6/MXene, nanostructure composite electrodes were subjected to the electrochemical impedance spectroscopy within frequency span of 1 Hz to 1 MHz. An AC amplitude of 5 mV was applied to a liquid electrolyte of 1 mol L^{-1} Na_2SO_4. Nyquist plots for the MXene, Bi_2MoO_6 and Bi_2MoO_6/MXene electrodes are depicted in Fig. 15e. Nyquist plots were used to compute charge-transfer resistance (R_1) and electrolyte resistance (R_2). The R_1 and R_2, C_{dl} and W values for MXene, Bi_2MoO_6 and Bi_2MoO_6/MXene electrodes determined from the Nyquist plots is shown in Table 5. Additionally, it was discovered thatBi_2MoO_6/MXenenanostructure composite electrodes demonstrated R_1, R_2 values of 6.84 Ω, 3.2 Ω, 2.02 mF and 43.8 mMho*s^0.5 respectively. Remarkably, Bi_2MoO_6/MXene electrode's R_1 and R_2 values were found to be nerly same those of MXene and Bi_2MoO_6 samples.

From this study it has been observed the impact of addition of MXene in Bi_2MoO_6 shows enhanced result. MXenes and MXene-based composites have a high specific energy, which makes them appropriate electrode materials for micro and flexible semiconductors. They also have excellent volumetric capacitance, pseudocapacitive behavior, cycle stability, and high-rate capability. Because to MXene's two-dimensional
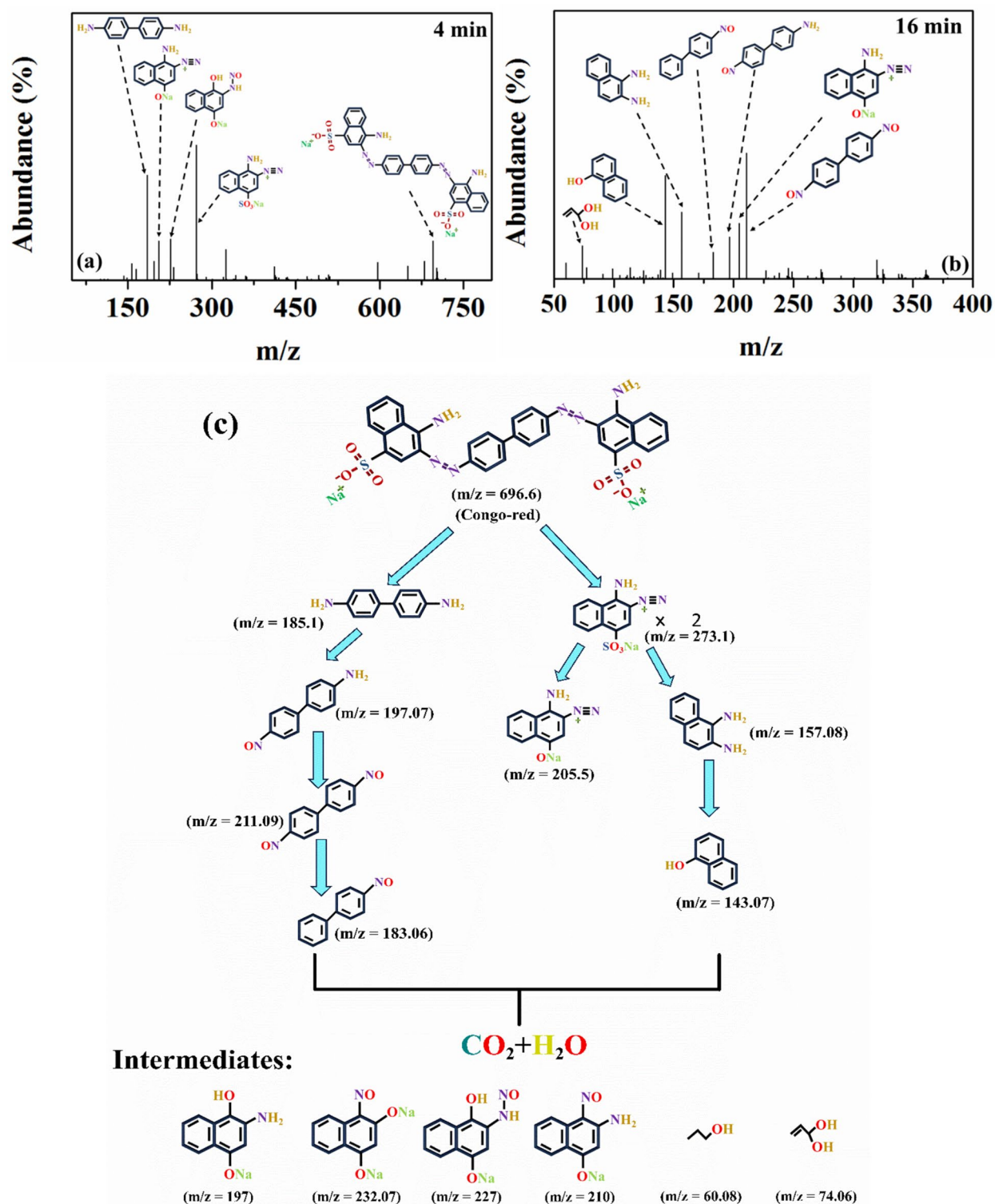
Fig. 13. (**a,b**) LC-HRMS spectra of Congo-red dye at 4 min and 16 min (**c**) along with the degradation pathway.

layer structure, ions such as H+ and Na+ can intercalate rapidly, facilitating effective storage of charging and performance in acidic electrolytes[61,62].

Conclusion

In summary, Bi_2MoO_6 nanostructures and their composite Bi_2MoO_6/MXene nanostructure were synthesized via hydrothermal methods to investigate their capabilities in photodegradation and energy storage. The Bi_2MoO_6/

Photocatalyst	% of degradation	Pollutants	Time (min)	References
BiOBr/Bi$_2$MoO$_6$	98.4%	Rhodamine B	120	63
MnFe$_2$O$_4$/Bi$_2$MoO$_6$/PPy	54.9%	Congo-red	120	64
NiO@Bi$_2$MoO$_6$–MoS	98.8%	Indigo carmine	120	65
Gd@Bi$_2$MoO$_6$/rGO	96.2%	Methylene Blue	120	66
	81.7%	Ciprofloxacin	120	66
BiOBr/Bi$_2$MoO$_6$@MXene	98%	Congo-red	480	67
TiO$_2$/Bi$_2$MoO$_6$	90.71%	Congo-red	80	68
	98.51%	Rhodamine B	100	68
Bi$_2$MoO$_6$/N-rGO	88%	Rhodamine B	30	69
	87%	Methylene Blue	30	69
Bi$_2$MoO$_6$/ZnSnO$_3$	95%	Methylene Blue	60	70
CdS/Bi$_2$MoO$_6$	88.7%	Rhodamine B	35	71
Bi$_2$MoO$_6$/MXene	92.3%	Congo-red	16	This work

Table 1. An overview of studies on photocatalytic degradation of dyes.

MXene composite exhibited rapid photodegradation, achieving 92.3% degradation of Congo Red dye within 16 min. This study emphasizes the importance of reducing the bandgap energy of materials through MXene incorporation to enhance photocatalytic performance. Verification of reactive agent and degradation pathways was accomplished through radical trapping tests and LC-HRMS analysis. Moreover, the composite showed a specific capacitance of 642.91 Fg^{-1}, energy density of 22.32 Wh kg^{-1}, and power density of 1.24 kW kg^{-1} at a current density of 5 Ag^{-1}, with 64.42% capacity retention at 20Ag^{-1} over 10,000 Galvanostatic charge-discharge cycles. These results suggest promising future applications in efficient photodegradation and advanced energy storage devices.
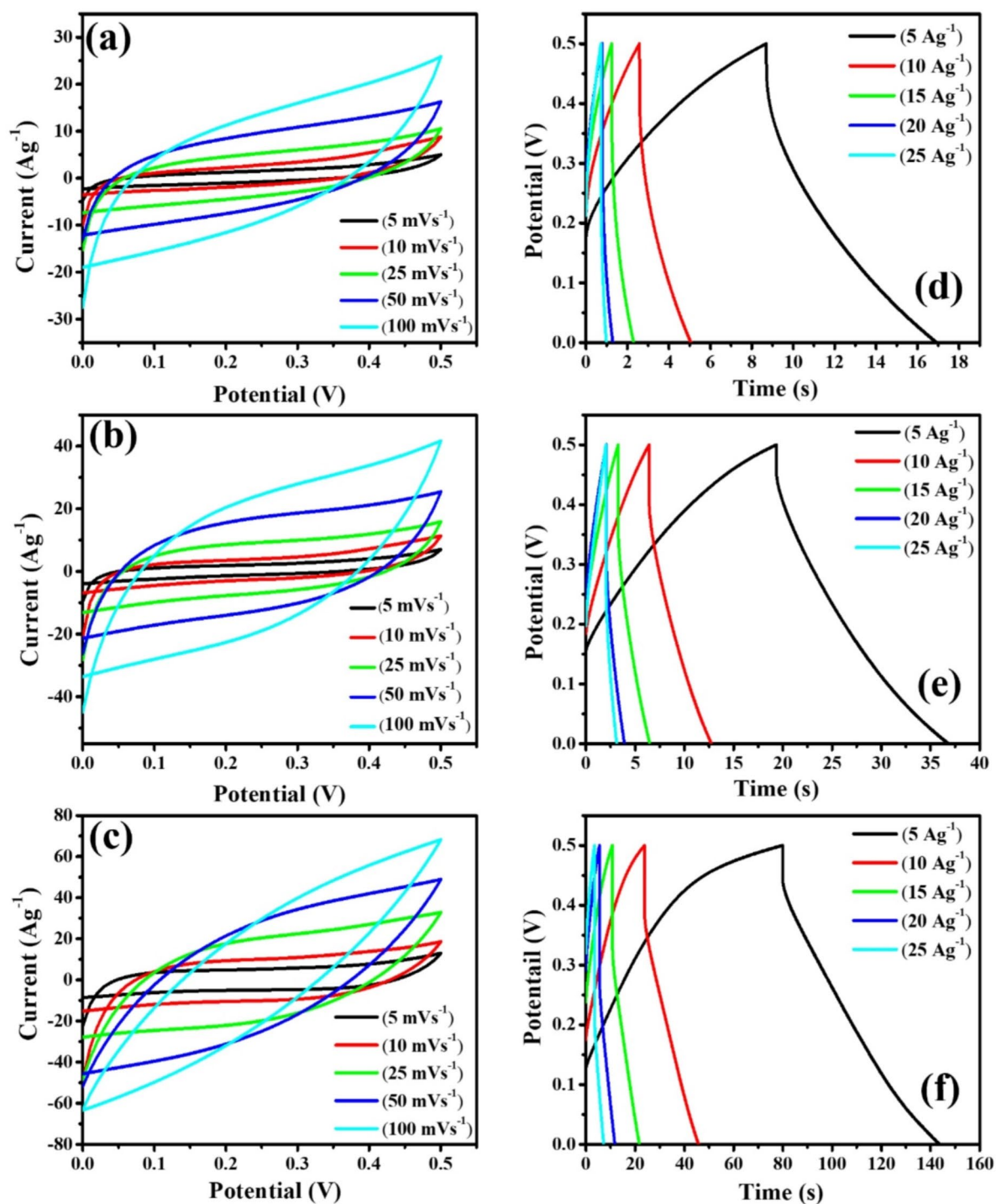
Fig. 14. (**a**–**c**) CV curves at different scan rates and (**d**–**f**) GCD curves at different current densities of MXene, Bi_2MoO_6 and Bi_2MoO_6/MXene electrodes.

Scan rate (mVs^{-1})	Specific capacitance (Fg^{-1})			Energy density (Whkg^{-1})		
	M	B	BM	M	B	BM
5	196.51	295.29	859.14	6.82	10.25	29.83
10	176.51	286.89	716.18	6.13	9.96	24.87
25	142.26	254.91	545.36	4.94	8.85	18.94
50	128.26	229.33	365.33	4.45	7.96	12.69
100	85.96	154.30	175.74	2.98	5.36	6.10

Table 2. The specific capacitance values at different scan rates for the MXene, Bi_2MoO_6 and Bi_2MoO_6/MXene electrodes calculated from CV curves. *M* MXene, *B* Bi_2MoO_6, *BM* Bi_2MoO_6/MXene.
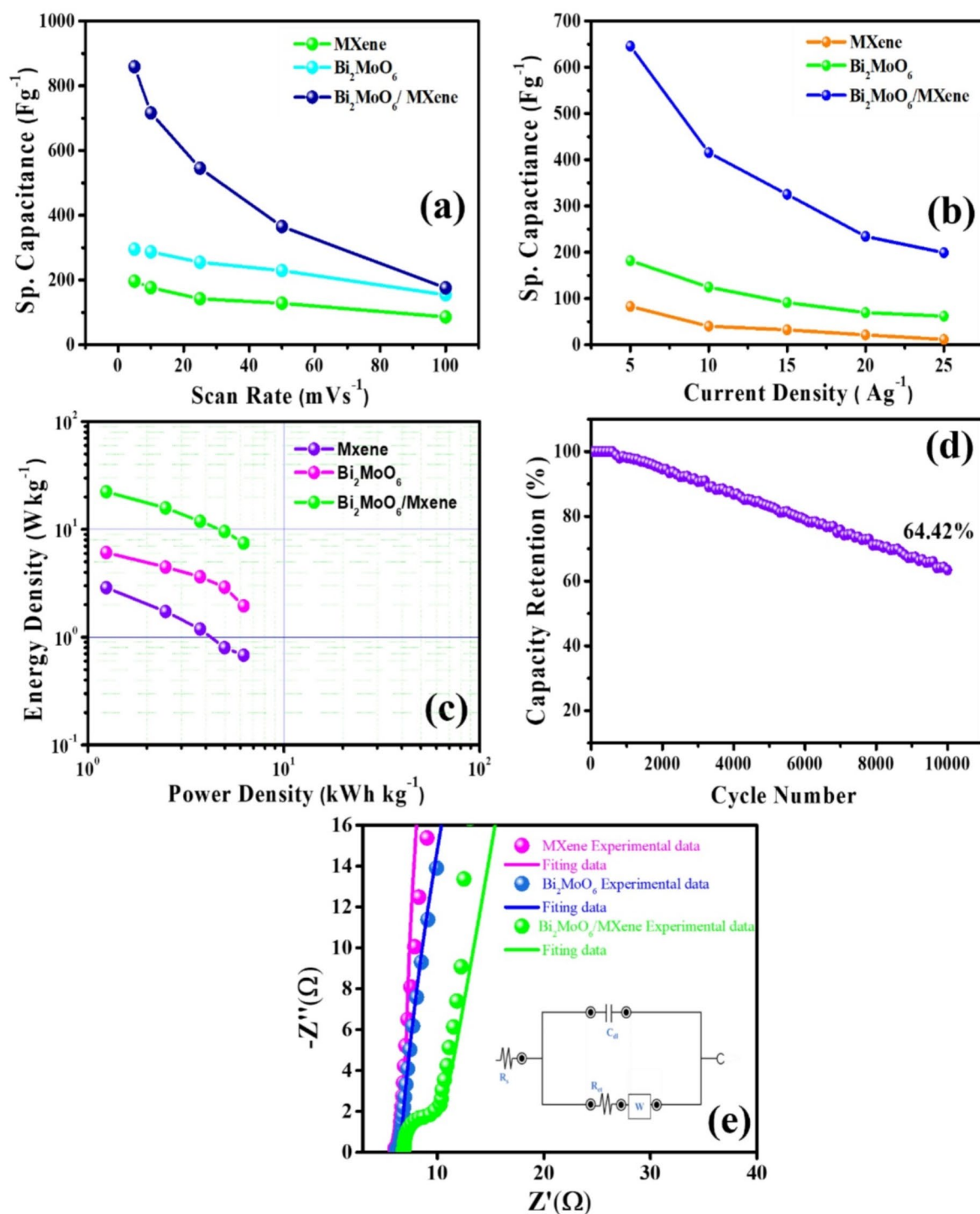
Fig. 15. (**a**) Variation in Cs vs. scan rate, (**b**) Variation in Cs with current densities, (**c**) Ragone plot of sample MXene, Bi_2MoO_6 and Bi_2MoO_6/MXene electrodes, and (**d**) capacity retention of Bi_2MoO_6/MXene electrode at constant current density of 20 Ag^{-1} (**e**) Nyquist plot (inset shows the equivalent circuit model for EIS data fitting) of MXene, Bi_2MoO_6 and Bi_2MoO_6/MXene electrodes.

Current density (Ag^{-1})	Specific capacitance (Fg^{-1})			Energy density (Whkg^{-1})			Power density (kWkg^{-1})		
	M	B	BM	M	B	BM	M	B	BM
5	83.22	175.83	642.91	2.88	6.10	22.32	1.24	1.24	1.24
10	50.05	129.01	455.61	1.73	4.47	15.81	2.49	2.49	2.49
15	34.43	104.75	342.24	1.19	3.63	11.88	3.74	3.74	3.74
20	23.32	83.54	275.79	0.80	2.90	9.57	4.99	4.99	4.99
25	19.205	56.28	215.04	0.66	1.95	7.46	6.24	6.24	6.24

Table 3. The specific capacitance values at different scan rates for the MXene, Bi_2MoO_6 and Bi_2MoO_6/MXene electrodes calculated from GCD curves. *M* MXene, *B* Bi_2MoO_6, *BM* Bi_2MoO_6/MXene.

Materials	Specific capacitance (Fg^{-1})	Current density (Ag^{-1})	Capacitance retention (%)/(cycles)	References
Carbon sphere@Bi_2MoO_6	521.42	1	78.9%/(10,000)	[72]
Hydrangea-type Bi_2MoO_6	485	5	82%/(5000)	[73]
mesoporous Bi_2MoO_6 quasi-nanospheres	345.0	1	90.2%/(10,000)	[74]
Bi_2MoO_6/Polyaniline	90.0	0.5	86.5%/(6000)	[75]
deoxyribonucleic acid -templated Bi_2MoO_6	467	2	86%/(3000)	[76]
Bi_2MoO_6 nanosheet	37.3	2	89%/(1,000)	[77]
N-Doped Carbon Dots/Bi_2MoO_6	184.2	1	87.3%/(10,000)	[15]
hierarchical Bi_2MoO_6 nanotubes	171.3	0.585	92.4%/(1000)	[78]
flowerlike Bi_2MoO_6	182	1	80%/(3000)	[79]
WO_3/Bi_2MoO_6/rGO	319	1	91%/(1000)	[19]
Bi_2MoO_6/MXene	645.7	5	64.4%/(10,000)	This work

Table 4. Compilation of recent studies on super capacitive performance of materials.

Electrode parameter	Mxene	$BiMoO_6$	$Bi2MoO6$/MXene
R_1	6 Ω	6.2 Ω	6.84
R_2	173 nΩ	273 nΩ	3.2Ω
C_{dl}	39.2 mF	13.3 mF	2.02 mF
W	7.68 mMho*s^0.5	5.78 mMho*s^0.5	43.8 mMho*s^0.5

Table 5. The R_1 and R_2 values for MXene, Bi_2MoO_6 and Bi_2MoO_6/MXene electrodes determined from the Nyquist plots.

Data availability
The datasets used and/or analyzed during the current study are available from the corresponding author on reasonable request.

References

1. Luo, Y. et al. A review on the occurrence of micropollutants in the aquatic environment and their fate and removal during wastewater treatment. *Sci. Total Environ.* **473–474**, 619–641 (2014).
2. Wang, L., Li, Y. & Han, P. Electrospinning preparation of g-C3N4/Nb2O5 nanofibers heterojunction for enhanced photocatalytic degradation of organic pollutants in water. *Sci. Rep.* 11, 1–12 (2021).
3. Akyon, B., McLaughlin, M., Hernández, F., Blotevogel, J. & Bibby, K. Characterization and biological removal of organic compounds from hydraulic fracturing produced water. *Environ. Sci. Process. Impacts.* **21**, 279–290 (2019).
4. Kamble, G. S. & Ling, Y. C. Solvothermal synthesis of facet-dependent BiVO4 photocatalyst with enhanced visible-light-driven photocatalytic degradation of organic pollutant: assessment of toxicity by zebrafish embryo. *Sci. Rep.* 10, 1–11 (2020).
5. Li, Q., Li, X., Wageh, S., Al-Ghamdi, A. A. & Yu, J. CdS/Graphene Nanocomposite Photocatalysts. *Adv. Energy Mater.* **5**, 1500010 (2015).
6. Chang, S., Yang, X., Sang, Y. & Liu, H. Highly efficient photocatalysts and continuous-Flow Photocatalytic reactors for degradation of Organic pollutants in Wastewater. *Chem. Asian J.* **11**, 2352–2371 (2016).
7. Maiti, S., Purakayastha, S. & Ghosh, B. Production of low-cost carbon adsorbents from agricultural wastes and their impact on dye adsorption. *Chem. Eng. Commun.* **195**, 386–403 (2008).
8. Siddiqui, S. I. et al. Investigation of Congo Red Toxicity towards different living organisms: a review. *Processes 2023.* **11, Page 807** (11), 807 (2023).

9. Bilal, M. et al. Photocatalytic degradation, toxicological assessment and degradation pathway of C.I. reactive blue 19 dye. *Chem. Eng. Res. Des.* **129**, 384–390 (2018).

10. Bilal, M., Asgher, M., Parra-Saldivar, R., ... H. H.-S. of the T. & 2017, undefined.Immobilized ligninolytic enzymes: an innovative and environmental responsive technology to tackle dye-based industrial pollutants–a review. *ElsevierM Bilal, M Asgher, R Parra-Saldivar, H Hu, W Wang, X Zhang, HMN IqbalScience of the Total Environment, 2017 Elsevier.*

11. Liu, L. et al. Metal nanoparticles induced photocatalysis. *Natl. Sci. Rev.* **4**, 761–780 (2017).

12. Luo, B., Liu, G. & Wang, L. Recent advances in 2D materials for photocatalysis. *Nanoscale.* **8**, 6904–6920 (2016).

13. Xie, W., Li, R. & Xu, Q. Enhanced photocatalytic activity of Se-doped TiO2 under visible light irradiation. *Sci. Rep.* **8**, 1–10 (2018).

14. Cronin, J., Anandarajah, G. & Dessens, O. Climate change impacts on the energy system: a review of trends and gaps. *Clim. Change.* **151**, 79–93 (2018).

15. Moorthi, K., Yesuraj, J., Kim, K. & Mohan, S. Electrochemical Performance of Chemically Integrated N-Doped Carbon Dots/Bi2MoO6 nanocomposites for symmetric supercapacitors. *Energy Fuels.* **37**, 6841–6853 (2023).

16. Thakur, Y. S. et al. Synthesis of 3D rice-like BiOCl battery-type electrode material and evaluation of their electrochemical performance in a symmetrical supercapacitor device configuration. *Mater. Sci. Semicond. Process.* **177**, 108376 (2024).

17. Karnan, M. et al. Nanoarchitechtonic marvels: Pioneering One-Pot synthesis of Bi2WO6 nanostructures for breakthrough in symmetric Supercapacitor Innovation. *ACS Appl. Energy Mater.* **7**, 5490–5500 (2024).

18. Manikandan, M. et al. Nickel-copper-cobalt mixed oxide electrode material for high performance asymmetric supercapacitor. *Sci. Rep.* **14**, 1–10 (2024).

19. Arooj, N. et al. Examining enhanced electrochemical performance through analysis of charge storage mechanisms in WO3/Bi2MoO6/rGO nanocomposites. *Mater. Sci. Engineering: B.* **306**, 117425 (2024).

20. Alonzo, S. M. M., Bentley, J., Desai, S. & Bastakoti, B. P. Hydrothermal synthesis of hierarchical microstructure tungsten oxide/carbon nanocomposite for supercapacitor application. *Sci. Rep.* **13**, 1–11 (2023).

21. Ahmed Alsharif, M., Alatawi, A., Hamdalla, T. A., Alfadhli, S. & Darwish, A. A. A. CuO nanoparticles mixed with activated BC extracted from algae as promising material for supercapacitor electrodes. *Sci. Rep.* **13**, 1–11 (2023).

22. Akkinepally, B. et al. Unlocking enhanced electrochemical performance of SnO2-Bi2WO6 nanoflowers for advanced supercapacitor device. *J. Alloys Compd.* **970**, 172677 (2024).

23. Bhat, A. et al. Prospects challenges and stability of 2D MXenes for clean energy conversion and storage applications. *NPJ 2D Materi. Appl.* **5**, 1–21 (2021).

24. Cai, T. et al. Ag3PO4/Ti3C2 MXene interface materials as a Schottky catalyst with enhanced photocatalytic activities and anti-photocorrosion performance. *Appl. Catal. B.* **239**, 545–554 (2018).

25. Kang, R. et al. Enhanced Thermal Conductivity of Epoxy Composites Filled with 2D Transition Metal Carbides (MXenes) with Ultralow Loading. *Sci. Rep.* **9**, 1–14 (2019).

26. Bai, S. et al. Recent advances of MXenes as electrocatalysts for hydrogen evolution reaction. *NPJ 2D Materi. Appl.* **5**, 1–15 (2021).

27. Rajapakse, M. et al. Intercalation as a versatile tool for fabrication, property tuning, and phase transitions in 2D materials. *NPJ 2D Materi. Appl.* **5**, 1–21 (2021).

28. Kumar, S. et al. Supercapacitors based on Ti3C2Tx MXene extracted from supernatant and current collectors passivated by CVD-graphene. *Sci. Rep.* **11**, 1–9 (2021).

29. Naguib, M., Mochalin, V. N., Barsoum, M. W. & Gogotsi, Y. 25th anniversary article: MXenes: a new family of two-dimensional materials. *Adv. Mater.* **26**, 992–1005 (2014).

30. Asaro, G. A. et al. MXene functionalized collagen biomaterials for cardiac tissue engineering driving iPSC-derived cardiomyocyte maturation. *NPJ 2D Mater. Appl.* **7**, 1–13 (2023).

31. Habib, T. et al. Oxidation stability of Ti3C2Tx MXene nanosheets in solvents and composite films. *NPJ 2D Mater. Appl.* **3**, 1–6 (2019).

32. Zhao, M. Q. et al. Flexible MXene/Carbon Nanotube Composite Paper with High Volumetric Capacitance. *Adv. Mater.* **27**, 339–345 (2015).

33. Syamsai, R. et al. Double transition metal MXene (TixTa4−xC3) 2D materials as anodes for Li-ion batteries. *Sci. Rep.* **11**, 1–13 (2021).

34. Tang, Q., Zhou, Z. & Shen, P. Are MXenes promising anode materials for Li ion batteries? Computational studies on electronic properties and Li storage capability of Ti 3 C 2 and Ti 3 C 2X 2 (X = F, OH) monolayer. *J. Am. Chem. Soc.* **134**, 16909–16916 (2012).

35. Chen, W. et al. Self-supported Bi2MoO6 nanosheet arrays as advanced integrated electrodes for li-ion batteries with super high capacity and long cycle life. *Nano* **13**, (2018).

36. Guo, M. et al. Bi2WO6–BiOCl heterostructure with enhanced photocatalytic activity for efficient degradation of oxytetracycline. *Sci. Rep.* **10**, 1–13 (2020).

37. Khazaee, Z., Mahjoub, A. R., Khavar, C., Srivastava, A. H., Sillanpää, M. & V. & Synthesis of layered perovskite Ag,F-Bi 2 MoO 6 /rGO: a surface plasmon resonance and oxygen vacancy promoted nanocomposite as a visible-light photocatalyst. *J. Photochem. Photobiol Chem.* **379**, 130–143 (2019).

38. Zhang, G. et al. Fabrication of Bi2MoO6/ZnO hierarchical heterostructures with enhanced visible-light photocatalytic activity. *Appl. Catal. B.* **250**, 313–324 (2019).

39. Global Solar Atlas. https://globalsolaratlas.info/map?c=28.611048,77.037849,11&s=28.610948,77.038456&m=site.

40. Rafiq, A. et al. Photocatalytic degradation of dyes using semiconductor photocatalysts to clean industrial water pollution. *J. Ind. Eng. Chem.* **97**, 111–128 (2021).

41. Naguib, M. et al. Two-dimensional nanocrystals produced by exfoliation of Ti(3)AlC(2). *Adv. Mater.* **37**, 4248–4253 (2011).

42. Sun, Y. et al. 2D MXenes as Co-catalysts in Photocatalysis: Synthetic Methods. *Nano-Micro Lett.* **11**, 1–22 (2019).

43. Mehlawat, S. et al. Next-generation BiOCl/MXene nanocomposites: optimized for dye removal and Supercapacitor Applications. *Langmuir.* https://doi.org/10.1021/ACS.LANGMUIR.4C03215 (2024).

44. Xie, W. et al. Insights into the atomic structure of oxygen vacancy on Bi2MoO6/MXene heterojunction and its role for boosting photocatalytic NO oxidation. *Appl. Surf. Sci.* **638**, 158104 (2023).

45. Zhang, X. et al. Enhancing the photocatalytic activity of Bi2MoO6 by constructing tailored composites through a turnable amount of MoS2. *J. Mater. Sci.: Mater. Electron.* **35**, 1–16 (2024).

46. Alhabeb, M. et al. Guidelines for synthesis and Processing of two-dimensional Titanium Carbide (Ti3C2Tx MXene). *Chem. Mater.* **29**, 7633–7644 (2017).

47. Jiang, X. et al. Inkjet-printed MXene micro-scale devices for integrated broadband ultrafast photonics. *MPJ 2D Mater. Appl.* **3**, 1–9 (2019).

48. Zhu, J., Tang, Y., Yang, C., Wang, F. & Cao, M. Composites of TiO 2 nanoparticles deposited on Ti 3 C 2 MXene nanosheets with enhanced Electrochemical Performance. *J. Electrochem. Soc.* **163**, A785–A791 (2016).

49. Han, M. et al. Ti3C2 MXenes with modified surface for high-performance electromagnetic absorption and shielding in the X-Band. *ACS Appl. Mater. Interfaces.* **8**, 21011–21019 (2016).

50. Yuan, S. et al. Self-assembled 3D hierarchical porous Bi2MoO6 microspheres toward high capacity and Ultra-long-life Anode Material for Li-Ion batteries. *ACS Appl. Mater. Interfaces.* **9**, 21781–21790 (2017).

51. Xu, X. et al. Highly intensified Molecular Oxygen activation on Bi@Bi2MoO6 via a metallic bi-coordinated facet-dependent effect. *ACS Appl. Mater. Interfaces.* **12**, 1867–1876 (2020).

52. Chen, Z. et al. Enhanced photocatalytic degradation of ciprofloxacin by heterostructured BiOCl/Ti3C2Tx MXene nanocomposites. *J. Alloys Compd.* **950**, 169797 (2023).
53. Singh, K. et al. Effect of the standardized ZnO/ZnO-GO filter element substrate driven Advanced Oxidation process on Textile Industry Effluent Stream: detailed analysis of Photocatalytic Degradation kinetics. *ACS Omega.* **8**, 28615–28627 (2023).
54. Di Mauro, A. et al. Novel synthesis of ZnO/PMMA nanocomposites for photocatalytic applications. *Sci. Rep.* **7**, 1–12 (2017).
55. Groeneveld, I., Kanelli, M., Ariese, F. & van Bommel, M. R. Parameters that affect the photodegradation of dyes and pigments in solution and on substrate – an overview. *Dyes Pigm.* **210**, 110999 (2023).
56. Yadav, P., Dhariwal, N., Kumari, M., Kumar, V. & Thakur, O. P. Enhanced degradation of Congo-red dye by Cr3 + doped α-Fe2O3 nano-particles under sunlight and industrial wastewater treatment. *Chemosphere* **343**, (2023).
57. Trenczek-Zajac, A. et al. Scavenger-supported photocatalytic evidence of an extended type I Electronic structure of the TiO2@Fe2O3Interface. *ACS Appl. Mater. Interfaces.* **14**, 38255–38269 (2022).
58. Mathew, S. et al. Synthesis, mechanisms, challenges, and future prospects of Ti3C2 MXene and its heterojunctions for photocatalytic dye degradation efficiency: a comprehensive review. *Mater. Today Sustain.* **24**, 100568 (2023).
59. Simon, P. & Gogotsi, Y. Materials for electrochemical capacitors. *Nat. Mater.* **7**, 845–854 (2008).
60. Conway, B. E. Electrochemical Supercapacitors. *Electrochemical Supercapacitors.* https://doi.org/10.1007/978-1-4757-3058-6 (1999).
61. Akhter, R., Maktedar, S. S. & MXenes: A comprehensive review of synthesis, properties, and progress in supercapacitor applications. *J. Materiomics.* **9**, 1196–1241 (2023).
62. Otgonbayar, Z., Yang, S., Kim, I. J. & Oh, W. C. Recent advances in two-dimensional MXene for Supercapacitor Applications: Progress, challenges, and perspectives. *Nanomaterials.* **13**, 919 (2023).
63. Wang, D., Shen, H., Guo, L., Wang, C. & Fu, F. Porous BiOBr/Bi2MoO6 heterostructures for highly selective adsorption of Methylene Blue. *ACS Omega.* **1**, 566–577 (2016).
64. Wang, Y., He, L., Dang, G., Li, H. & Li, X. Polypyrrole-functionalized magnetic Bi2MoO6 nanocomposites as a fast, efficient and reusable adsorbent for removal of ketoprofen and indomethacin from aqueous solution. *J. Colloid Interface Sci.* **592**, 51–65 (2021).
65. Nandisha, P. S., Yallappa, S. & Sowbhagya & Synthesis and characterization of ternary NiO@Bi2MoO6–MoS heterojunction with enhanced photodegradation efficiency towards indigo carmine dye. *Solid State Sci.* **139**, 107157 (2023).
66. Ahmad, Z. et al. Fine-tuning of redox-ability, optical, and electrical properties of Bi2MoO6 ceramics via lanthanide doping and rGO integration for photo-degradation of Methylene Blue and Ciprofloxacin. *J. Alloys Compd.* **1002**, 175466 (2024).
67. Yang, Z. et al. Ternary hetero-structured BiOBr/Bi2MoO6@MXene composite membrane: construction and enhanced removal of antibiotics and dyes from water. *J. Memb. Sci.* **669**, 121329 (2023).
68. Wu, J. et al. A stable and regenerative TiO2/Bi2MoO6 photocatalyst for highly effective degradation of rhodamine B and Congo Red. *Int. J. Environ. Anal. Chem.* https://doi.org/10.1080/03067319.2024.2376901 (2024).
69. Kasinathan, M. et al. Fabrication of novel Bi2MoO6/N-rGO catalyst for the efficient photocatalytic degradation of harmful dyes. *Mater. Res. Bull.* **125**, 110782 (2020).
70. Liu, Y., Yang, Z. H., Song, P. P., Xu, R. & Wang, H. Facile synthesis of Bi2MoO6/ZnSnO3 heterojunction with enhanced visible light photocatalytic degradation of methylene blue. *Appl. Surf. Sci.* **430**, 561–570 (2018).
71. Feng, Y. et al. Hydrothermal synthesis of CdS/Bi2MoO6 heterojunction photocatalysts with excellent visible-light-driven photocatalytic performance. *Appl. Surf. Sci.* **353**, 87–94 (2015).
72. Samdani, K. J., Park, J. H., Joh, D. W. & Lee, K. T. Self-assembled Bi2MoO6 nanopetal array on Carbon spheres toward enhanced Supercapacitor Performance. *ACS Sustain. Chem. Eng.* **6**, 16702–16712 (2018).
73. Shinde, P. V., Shinde, N. M., Yun, J. M., Mane, R. S. & Kim, K. H. Facile Chemical synthesis and potential Supercapattery Energy Storage Application of Hydrangea-type Bi2MoO6. *ACS Omega.* **4**, 11093–11102 (2019).
74. Wang, L. et al. Mesoporous Bi2MoO6 quasi-nanospheres anchored on activated carbon cloth for flexible all-solid-state supercapacitors with enhanced energy density. *J. Power Sources.* **463**, 228202 (2020).
75. Wu, F. et al. Synthesis and characterization of hierarchical Bi2MoO6/Polyaniline nanocomposite for all-solid-state asymmetric supercapacitor. *Electrochim. Acta.* **245**, 685–695 (2017).
76. Yesuraj, J., Austin Suthanthiraraj, S. & Padmaraj, O. Synthesis, characterization and electrochemical performance of DNA-templated Bi2MoO6 nanoplates for supercapacitor applications. *Mater. Sci. Semicond. Process.* **90**, 225–235 (2019).
77. Ma, Y. et al. Facile growth of Bi2MoO6 nanosheet arrays on ni foam as an electrode for electrochemical applications. *RSC Adv.* **6**, 12093–12099 (2016).
78. Ma, Y. et al. Hierarchical nanosheet-based Bi2MoO6 nanotubes with remarkably improved electrochemical performance. *J. Power Sources.* **331**, 481–486 (2016).
79. Yu, T. et al. Facile synthesis of Flowerlike Bi2MoO6 Hollow microspheres for high-performance supercapacitors. *ACS Sustain. Chem. Eng.* **6**, 7355–7361 (2018).

Author contributions

Declarations

Competing interests
The authors declare no competing interests.

Additional information
Correspondence and requests for materials should be addressed to A.S.

Reprints and permissions information is available at www.nature.com/reprints.

Publisher's note Springer Nature remains neutral with regard to jurisdictional claims in published maps and institutional affiliations.